The Astrophysical Journal, 870:7 (16pp), 2019 January 1 https://doi.org/10.3847/1538-4357/aaeed0

Spectroscopic Confirmation of Five Galaxy Clusters at $z > 1.25$ in the 2500 deg^2 SPT-SZ Survey

G. Khullar[1,2], L. E. Bleem[2,3], M. B. Bayliss[4], M. D. Gladders[1,2], B. A. Benson[1,2,5], M. McDonald[4], S. W. Allen[6,7,8], D. E. Applegate[2], M. L. N. Ashby[9], S. Bocquet[3], M. Brodwin[10], E. Bulbul[9], R. E. A. Canning[7,8], R. Capasso[11,12], I. Chiu[13], T. M. Crawford[1,2], T. de Haan[14], J. P. Dietrich[11,12], A. H. Gonzalez[15], J. Hlavacek-Larrondo[16], H. Hoekstra[17], W. L. Holzapfel[14], A. von der Linden[18], A. B. Mantz[7,8], S. Patil[19], C. L. Reichardt[19], A. Saro[20], K. Sharon[21], B. Stalder[22], S. A. Stanford[23], A. A. Stark[9], and V. Strazzullo[11]

[1] Department of Astronomy and Astrophysics, University of Chicago, 5640 South Ellis Avenue, Chicago, IL 60637, USA; gkhullar@uchicago.edu
[2] Kavli Institute for Cosmological Physics, University of Chicago, 5640 South Ellis Avenue, Chicago, IL 60637, USA
[3] Argonne National Laboratory, High-Energy Physics Division, 9700 S. Cass Avenue, Argonne, IL 60439, USA
[4] Kavli Institute for Astrophysics & Space Research, Massachusetts Institute of Technology, 77 Massachusetts Avenue, Cambridge, MA 02139, USA
[5] Fermi National Accelerator Laboratory, Batavia, IL 60510-0500, USA
[6] SLAC National Accelerator Laboratory, 2575 Sand Hill Road, Menlo Park, CA 94025, USA
[7] Kavli Institute for Particle Astrophysics and Cosmology, Stanford University, 452 Lomita Mall, Stanford, CA 94305, USA
[8] Department of Physics, Stanford University, 382 Via Pueblo Mall, Stanford, CA 94305, USA
[9] Harvard-Smithsonian Center for Astrophysics, 60 Garden Street, MS 66, Cambridge, MA 02138, USA
[10] Department of Physics and Astronomy, University of Missouri, 5110 Rockhill Road, Kansas City, MO 64110, USA
[11] Faculty of Physics, Ludwig-Maximilians-Universität, Scheinerstr. 1, D-81679 Munich, Germany
[12] Excellence Cluster Universe, Boltzmannstr. 2, D-85748 Garching, Germany
[13] Academia Sinica Institute of Astronomy and Astrophysics, 11F of AS/NTU Astronomy-Mathematics Building, No.1, Sec. 4, Roosevelt Road, Taipei 10617, Taiwan
[14] Department of Physics, University of California, Berkeley, CA 94720, USA
[15] Department of Astronomy, University of Florida, Gainesville, FL 32611, USA
[16] Department of Physics, University of Montreal, Montreal, QC H3C 3J7, Canada
[17] Leiden Observatory, Leiden University, Niels Bohrweg 2, 2333 CA, Leiden, The Netherlands
[18] Department of Physics and Astronomy, Stony Brook University, Stony Brook, NY 11794, USA
[19] School of Physics, The University of Melbourne, Parkville, VIC 3010, Australia
[20] INAF-Observatorio Astronomico di Trieste, via G.B. Tiepolo 11, I-34143 Trieste, Italy
[21] Department of Astronomy, University of Michigan, 1085 South University Drive, Ann Arbor, MI 48109, USA
[22] LSST, 950 North Cherry Avenue, Tucson, AZ 85719, USA
[23] Physics Department, University of California, Davis, CA 95616, USA

Received 2018 June 5; revised 2018 October 31; accepted 2018 November 4; published 2018 December 27

Abstract

We present spectroscopic confirmation of five galaxy clusters at $1.25 < z < 1.5$, discovered in the 2500 deg^2 South Pole Telescope Sunyaev–Zel'dovich (SZ) survey. These clusters, taken from a mass-limited sample with a nearly redshift-independent selection function, have multiwavelength follow-up imaging data from the X-ray to near-IR and currently form the most homogeneous massive high-redshift cluster sample known. We identify 44 member galaxies, along with 25 field galaxies, among the five clusters, and describe the full set of observations and data products from Magellan/LDSS3 multiobject spectroscopy of these cluster fields. We briefly describe the analysis pipeline and present ensemble analyses of cluster member galaxies that demonstrate the reliability of the measured redshifts. We report $z = 1.259$, 1.288, 1.316, 1.401, and 1.474 for the five clusters from a combination of absorption-line (Ca II H&K doublet—$\lambda\lambda$3968, 3934) and emission-line ([O II] $\lambda\lambda$3727, 3729) spectral features. Moreover, the calculated velocity dispersions yield dynamical cluster masses in good agreement with the SZ masses for these clusters. We discuss the velocity and spatial distributions of passive and [O II]-emitting galaxies in these clusters, showing that they are consistent with velocity segregation and biases observed in lower redshift South Pole Telescope clusters. We identify modest [O II] emission and pronounced CN and Hδ absorption in a stacked spectrum of 28 passive galaxies with Ca II H&K-derived redshifts. This work increases the number of spectroscopically confirmed SZ-selected galaxy clusters at $z > 1.25$ from three to eight, further demonstrating the efficacy of SZ selection for the highest redshift massive clusters and enabling detailed study of these systems.

Key words: galaxies: clusters: general – galaxies: distances and redshifts – galaxies: evolution – galaxies: kinematics and dynamics – galaxies: high-redshift

1. Introduction

From overdensities in the initial matter distribution in the universe, galaxy clusters form and evolve into the massive structures that we observe today. Clusters sample a broad range of galaxy overdensities and mass accretion histories, and studies of these systems provide insight into how stars form and assemble within galaxies, and the evolutionary paths that member galaxies take in cluster environments (Oemler 1974; Dressler 1980; Dressler & Gunn 1983; Balogh et al. 1997; Blanton & Moustakas 2009).

Observations of galaxy clusters at $z < 1$ suggest that galaxies in clusters form stars in an epoch of early and rapid star formation (at $z > 3$), before quickly settling into a mode of passive and stable evolution (Stanford et al. 1998, 2005; Holden et al. 2005; Mei et al. 2006). Thus, observations of

Table 1
Galaxy Clusters in the SPT-SZ High-z Cluster Sample[a]

Cluster ID (SPT Cat.) (1)	R.A. J2000 (2)	Decl. J2000 (3)	ξ[a] (SZ Significance) (4)	Redshift (Photometric or Previously Published) (5)	M_{500c} $10^{14}\ h_{70}^{-1}\ M_{\odot}$ (6)
SPT-CL J2341-5724	355.3568	−57.4158	6.87	1.38 ± 0.08	3.05 ± 0.60
SPT-CL J0156-5541	29.0449	−55.6980	6.98	1.22 ± 0.08	3.63 ± 0.70
SPT-CL J0640-5113	100.0645	−51.2204	6.86	1.25 ± 0.08	3.55 ± 0.70
SPT-CL J0607-4448	91.8984	−44.8033	6.44	1.43 ± 0.09	3.14 ± 0.64
SPT-CL J0313-5334	48.4809	−53.5781	6.09	1.37 ± 0.09	2.97 ± 0.64
SPT-CL J0205-5829	31.4428	−58.4852	10.50	1.322[b]	4.74 ± 0.77
SPT-CL J2040-4451	310.2483	−44.8602	6.72	1.478[c]	3.33 ± 0.66
SPT-CL J0459-4947	74.9269	−49.7872	6.29	1.70 ± 0.02[d]	2.67 ± 0.55

Notes. Galaxy clusters in bold are analyzed in this paper.
[a] From Bleem et al. (2015). See Section 2.1 for more details.
[b] Spectroscopic follow-up in Stalder et al. (2013).
[c] Spectroscopic follow-up in Bayliss et al. (2014).
[d] Preliminary result from A. B. Mantz et al. (2018, in preparation).

clusters at higher redshifts should sample an epoch where this star formation—or at least its end stages—is observed in situ. Recent studies of modest heterogeneous samples of galaxy clusters at $1 < z < 2$ have shown high star formation and active galactic nucleus (AGN) activity compared with lower redshifts, and a luminosity function that is evolving (Hilton et al. 2009; Mancone et al. 2010, 2012; Tran et al. 2010; Fassbender et al. 2011; Snyder et al. 2012; Zeimann et al. 2012; Brodwin et al. 2013; Alberts et al. 2014, 2016). This is evidence that galaxy clusters are undergoing significant mass assembly in this epoch, inviting further investigation into properties of member galaxies and the intracluster medium (ICM) at $z > 1$.

Although massive clusters are easy to observe in the local universe, the discovery of clusters with similar properties in the high-redshift universe is still technically challenging. This is due to two main reasons. First, optical and X-ray fluxes—which are observational tracers of galaxy clusters—decrease at cosmological distances (due to cosmological dimming). Second, massive galaxy clusters are extremely rare at higher redshifts. Thus, surveys that aim to find distant clusters by directly detecting emission from either the ICM or member galaxies must be both wide and deep. Despite these obstacles, the current status of observations in the $z > 1$ regime is promising, and the science is transforming from the characterization of individual objects to comprehensive analyses of statistically well-defined samples of clusters. A combination of deep X-ray observations (Rosati et al. 2004, 2009; Mullis et al. 2005; Stanford et al. 2006; Culverhouse et al. 2010; Bartalucci et al. 2018) and optical + near-infrared (IR) imaging and spectroscopy (Stanford et al. 2005, 2012, 2014; Brodwin et al. 2006, 2011; Elston et al. 2006; Wilson et al. 2006; Eisenhardt et al. 2008; Muzzin et al. 2009; Demarco et al. 2010; Papovich et al. 2010; Santos et al. 2011; Gettings et al. 2012; Zeimann et al. 2012; Gonzalez et al. 2015; Balogh et al. 2017; Paterno-Mahler et al. 2017) has improved our understanding of galaxy clusters that have large X-ray, optical, and IR fluxes at $1 < z < 2$.

It is also worth noting that these wavelength regimes have their unique advantages. Optical and IR surveys target galaxy overdensities and can probe to low mass thresholds for systems with a breadth of dynamical states and star formation histories. X-ray observations of clusters provide us with direct measurement of the ICM temperature and electron density, a tracer of cluster mass that is readily captured in cosmological simulations. However, one challenge with optical and IR surveys is whether the selection of galaxy clusters based on galaxies systematically affects the studies of member galaxy properties. To robustly study cluster galaxies absent this concern, an ICM-selected sample is appropriate.

Sunyaev–Zel'dovich effect (SZE) cluster surveys from the *Planck* mission (Planck Collaboration et al. 2014), Atacama Cosmology Telescope (ACT; Sifón et al. 2016; Hilton et al. 2018), and the South Pole Telescope (SPT; Bleem et al. 2015, hereafter B15) offer a new opportunity to study galaxy clusters selected by their ICM signal. Both ACT and SPT provide a nearly redshift-independent, mass-limited sample of clusters, due to their arcminute angular resolution, which is well matched to cluster sizes, with a mass threshold set by the sensitivity of the instruments (Carlstrom et al. 2002). Of these, only the South Pole Telescope Sunyaev–Zel'dovich (SPT-SZ) cluster catalog yields a significant sample of $z > 1$ clusters.

The 2500 deg^2 SPT-SZ survey catalog contains 677 galaxy cluster candidates with a statistical significance >4.5, with 37 at $z > 1$ (B15) based primarily on photometric red-sequence redshifts. Spectroscopic confirmations along with astrophysical and cosmological analyses of multiple high-redshift and massive galaxy clusters from the SPT-SZ survey, many unique to the SPT-SZ sample, have been previously published (Brodwin et al. 2010; McDonald et al. 2013, 2017; Stalder et al. 2013; Bayliss et al. 2014, 2016; Ruel et al. 2014). This includes spectroscopic confirmation of two particularly distant massive clusters at $z = 1.322$ (Stalder et al. 2013) and $z = 1.478$ (Bayliss et al. 2014). This paper provides spectroscopic confirmation and optical–NIR spectroscopic follow-up of a further five SPT-SZ clusters at $1.25 < z < 1.5$.

This paper is organized as follows. Section 2 describes the sample selection, optical–NIR imaging, and optical spectroscopy used to derive spectroscopic redshifts for the clusters. In Section 3, we describe the spectral analysis performed on the data from member galaxies of the sample population, while Section 4 describes the resulting spectroscopic redshifts and confirmation of

member galaxies. In Section 5, we consider several analyses of these data, cluster velocity dispersions, a stacked velocity–radius diagram, and a stacked spectral analysis, all of which demonstrate —despite the challenge presented by spectroscopy of individual member galaxies in these distant systems—that the spectroscopic results are as expected. We summarize our results in Section 6.

Magnitudes in this work have been calibrated with respect to Vega. The fiducial cosmology model used for all distance measurements as well as other cosmological values assumes a standard flat cold dark matter universe with a cosmological constant (ΛCDM) $H_0 = 70\,\mathrm{km\,s^{-1}\,Mpc^{-1}}$ and matter density $\Omega_M = 0.30$. All Sunyaev–Zel'dovich (SZ) significance-based masses from B15 are reported in terms of $M_{500c,\mathrm{SZ}}$, i.e., the SZ mass within R_{500c}, defined as the radius within which the mean density ρ is 500 times the critical density ρ_c of the universe.

2. Observations and Data

2.1. Cluster Sample Selection and Imaging Follow-up

The 2500 deg^2 SPT-SZ survey (Carlstrom et al. 2011), completed in 2011, discovered 37 galaxy clusters with high significance at $z > 1$, via the SZE. These clusters were detected via the SPT-SZ campaign that observed the CMB at frequencies of 95, 150, and 220 GHz. The full cluster catalog, B15, is ~100% complete at $z > 0.25$ for a mass threshold of $M_{500c} \geqslant 7 \times 10^{14} M_\odot h_{70}^{-1}$. Survey strategy and analysis details can be found in previous works by the SPT collaboration (Staniszewski et al. 2009; Vanderlinde et al. 2010; Williamson et al. 2011; Reichardt et al. 2013).

For optical and near-IR (NIR) photometric follow-up of this cluster sample, several programs were initiated (see Song et al. 2012 and B15 for details on observational strategies). Optical photometry in the *griz* bands was obtained for the sample clusters using either the CTIO (4 m) facility, ESO/New Technology Telescope (NTT, 3.58 m) or the Magellan/Baade Telescope (6.5 m) in Chile to depths that can detect galaxies at $0.4L_*$ at $z = 0.75$ at 5σ in red bands. This was followed up by *Spitzer*/IRAC observations in the 3.6 and 4.5 μm bands for NIR photometry, which is crucial for observations of higher redshift clusters for member galaxy candidate selection. The final NIR images detect $z = 1.5$ $0.4L_*$ galaxies at a 10σ significance.

The IR and optical photometry is complemented by observations in the *J*, *H*, *H*-long and K_s bands (the last two being modified versions of the standard *H* and *K* filters, respectively), using the wide-area near-IR instrument FOURSTAR on the Magellan/Baade telescope (Foreman-Mackey et al. 2013). Data were acquired between 2014 January and 2016 January; the data used here are a small subset of the overall data set, with details of the reduction and analysis to be provided in a future paper (M. B. Bayliss et al. 2018, in preparation). Deep optical photometric follow-up was also acquired for four of the five clusters discussed in this paper using the simultaneous *griz* imager Magellan/PISCO (Stalder et al. 2014) on 2016 November 2. Deep *HST*/WFC3 photometry in the F814W and F140W filters (PI: Strazzullo, *HST* Cycle 23 program) is available for the fifth cluster, SPT-CL J0607-4448. RGB images for the sample clusters are shown in Figure 1.

The cluster subsample analyzed in detail here comprises five of the eight most massive $z > 1.2$ clusters from the SPT-SZ sample, all of which have deep *Chandra* X-ray imaging (McDonald et al. 2017). The remaining three are SPT-CL J2040-5541 (spectroscopically confirmed at $z = 1.478$ in Bayliss et al. 2014), SPT-CL J0205-5829 (spectroscopically confirmed at $z = 1.322$ in Stalder et al. 2013), and SPT-CL J0459-4947, for which current data provide an X-ray spectroscopic redshift of 1.70 ± 0.02 (A. B. Mantz et al. 2018, in preparation, with a past published redshift of 1.85 in McDonald et al. 2017). This total sample is referred to as the "SPT High-z Cluster" sample.

Table 2
Photometric Data in this Study

Cluster Name (1)	Imaging (RGB) (Telescope and Instrument) (2)
SPT-CL J2341-5724	*Spitzer*/IRAC 3.6 μm
	Magellan/FOURSTAR *J*
	Magellan/PISCO z
SPT-CL J0156-5541	*Spitzer*/IRAC 3.6 μm
	Magellan/FOURSTAR *H*
	Magellan/PISCO z
SPT-CL J0640-5113	*Spitzer*/IRAC 3.6 μm
	Magellan/FOURSTAR *J*
	Magellan/PISCO z
SPT-CL J0607-4448	*Spitzer*/IRAC 3.6 μm
	Magellan/FOURSTAR *J*
	ESO/NTT z
SPT-CL J0313-5334	*Spitzer*/IRAC 3.6 μm
	Magellan/FOURSTAR K_s
	Magellan/PISCO z

Note. See Section 2.1 for more details on imaging follow-up of sample clusters.

In Section 2.2, we describe the spectroscopic optical observations of this five-cluster subsample. The cataloged properties of these five clusters, and the further three systems that complete the set of the most massive high-redshift clusters in the SPT-SZ sample, are reproduced from B15 in Table 1. The photometric data used for constructing RGB images in this work are summarized in Table 2.

2.2. Spectroscopy: Optical and Near-IR

2.2.1. Spectral Observations

The primary motivation for optical and NIR follow-up of this cluster sample is securing spectroscopic redshifts of clusters and their member galaxies. Optical spectroscopy of these five clusters was carried out between 2014 August and 2015 January on the 6.5 m Magellan/Clay Telescope using the 600 lines/mm VPH-Red grism on the Low Dispersion Survey Spectrograph[24]—3C (LDSS3C) in Normal mode (as opposed to nod and shuffle). These data represent some of the earliest spectroscopy acquired with the new LDSS3C system and include both unfiltered spectra and spectra acquired using the OG590 order separating filter—the latter being used to remove second-order contamination in cluster spectra where imaging showed higher blue-end flux.

The slits for target galaxy spectra were typically cut 6″ long (along the spatial axis) on the mask and 1″ wide (along the dispersion axis); LDSS3C has a scale of 0.″188/pixel. In most instances, the target galaxy was positioned at the slit center, with some misalignment on the spatial axis tolerated in order to optimize slit packing. Square boxes, typically six per mask,

[24] http://www.lco.cl/Members/gblanc/ldss-3/ldss-3-user-manual-tmp

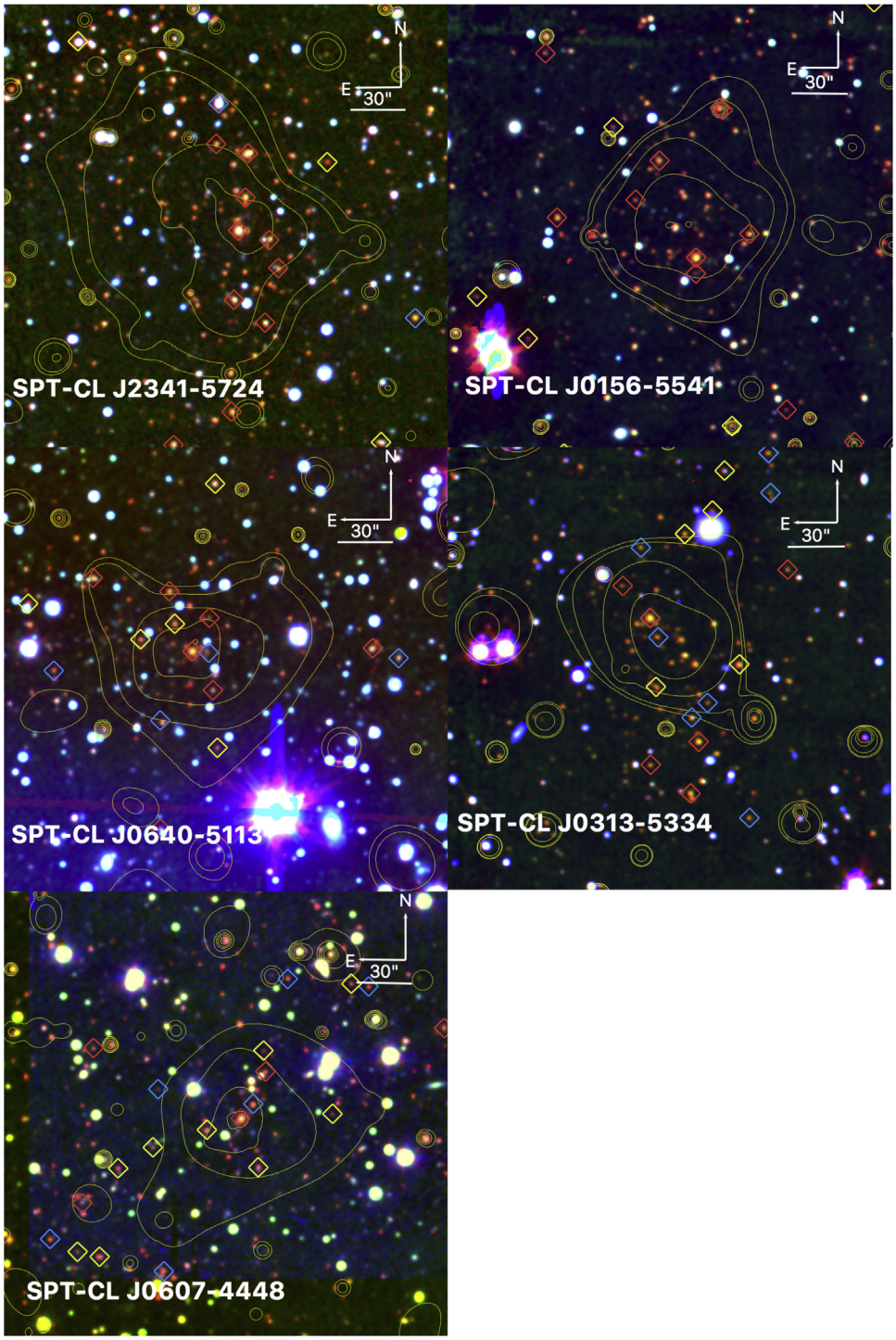

Figure 1. RGB $4' \times 4'$ images for the sample clusters. Data are *Spitzer* IRAC 3.6 μm (red channel), Magellan/FOURSTAR *J, H*, or K_s (green channel), and Magellan/PISCO z (blue channel), except for SPT-CL J0607-4448, for which the blue channel is ESO/NTT z-band data. Images are centered on their SZ centers. Diamonds indicate all objects targeted for spectroscopic observations. Red diamonds indicate spectroscopically confirmed cluster members (see Sections 3 and 4). Yellow diamonds indicate objects for which no redshifts could be measured, while blue diamonds indicate confirmed field galaxies. Contours are drawn from smoothed *Chandra* X-ray data for these clusters (McDonald et al. 2017), spaced equally in $\log_{10}$(flux) from the lowest discernible value that isolates the cluster, up to just beyond the peak of diffuse emission from the cluster.

were used to target nearby stars for mask alignment on the sky. Spectra of individual galaxies typically cover the wavelength range 7500–10000 Å, with a typical exposure time of 7200 s and an observation airmass of ∼1.2–1.5. The typical seeing during the observations was $\sim 1''$.

2.2.2. Designing Spectroscopic Masks

Potential red-sequence cluster members were targeted first for slit placement, selected by apparent color, brightness, morphology, and their proximity to the SZ center and galaxy overdensity. Further slits were placed on fainter or bluer galaxies.

Some spatial misalignment (∼1/10th of an arcsecond) was allowed to optimize slit packing. This process typically results in an elongated (rather than circular) layout of targeted galaxies, as can be seen in Figure 1. In most cases, a slit was placed on any apparent brightest cluster galaxy (BCG).

3. Spectral Analysis

3.1. Spectra Reduction

The spectra were processed using The Carnegie Observatories System for Multi-Object Spectroscopy (COSMOS)[25] reduction package, which is specifically designed to reduce raw spectra acquired using the Magellan Telescopes.

We describe the data reduction briefly below. All images were de-biased using bias frames acquired each afternoon. We used a HeNeAr comparison arc line for wavelength calibration. The analysis is focused on the range where the VPH-red grism is most sensitive and over which we expect useful features from red member galaxies: 7500–10000 Å. A flat-field image acquired temporally adjacent to each science frame was used to define the spectral trace for each slit. This flat image was also used to flat-field the slit response. Sky subtraction was performed by fitting a one-dimensional third-order spline along the dispersion axis, following the techniques outlined in Kelson (2003). Different exposures of the sky-subtracted science spectra were stacked and 2D cosmic-ray cleaning was performed by outlier rejection. COSMOS also generates a noise image that is dominated by photon noise in bright sky lines at these wavelengths.

Figure 2 shows examples of 2D sky-subtracted spectra from four potential member galaxies of the galaxy cluster SPT-CL 0156–5541. The *y*-axis depicts the spatial width of individual slits, against the horizontal dispersion axis (or wavelength), over the wavelength range 8500–9200 Å. Emission features ([O II] λ3727, 2729 doublet) and a strong spectral continuum can be clearly seen in some cases. It is crucial to note that there are sections of the spectra in the wavelength range of interest that are dominated by poor sky subtraction with significant systematics. A thorough exploration of the tunable parameters available in the COSMOS reduction package did little to ameliorate this—the poor sky subtraction is not due to an insufficient description of the slit geometry. In principle, fringing could contribute to this effect, but the LDSS3C detector is a thick, fully depleted CCD, the same as the chips used in the Dark Energy Camera (Flaugher et al. 2015), and is not expected to show fringing at this level. Our current understanding is that these artifacts are predominantly the result of slit roughness and are not fully removed by flat-fielding because the roughness produces both a transmission variation and small-scale variation in the wavelength solution. The quality of 2D spectra is a major factor in selecting analysis strategies for 1D spectra, which are described in the following sections.

3.2. One-dimensional Spectra

Two-dimensional spectra are condensed into one-dimensional spectra for analysis using the IRAF/NOAO package apall that fits polynomial functions to the spectral continuum (along the dispersion axis) in individual 2D spectra. Along the spatial axis, the process involved clipping slit edges for defects and fitting a boxcar model to the counts distribution. At any wavelength, the root mean square (rms) of the sky-subtracted residuals defines the uncertainties.

[25] http://code.obs.carnegiescience.edu/cosmos

3.3. Extracting Redshifts and Spectral Features

Due to suboptimal sky subtraction in the LDSS3 pipeline, the resulting 1D wavelength-calibrated (albeit not flux-calibrated) spectra are dominated by systematic noise at some wavelengths and are not suitable for sophisticated spectral analysis techniques that can be employed to analyze galaxy spectra (e.g., principal-component analysis). Several strong spectral features are apparent in some spectra, and we base much of the analysis that follows on the detection of these features, namely the [O II] $\lambda\lambda$3727, 3729 doublet emission lines and Ca II H&K $\lambda\lambda$3968, 3934 absorption lines. Atomic spectral features like [O II], [O III], and Hβ (more on this in Section 5.5) trace the direct light from excited nebular gas around young O, B stars that is unobscured by dust in star-forming regions in galaxies. Atomic Ca II H&K and molecular CN ((0, 0) violet 3850–3880 Å; also discussed in Section 5.5) features are pronounced in K stars in galaxies, tracing older stellar populations in galactic environments. For more details, we refer the reader to Bruzual & Charlot (1993).

Twenty-eight out of forty-four galaxies were confirmed via Ca II H&K, while 16 redshifts were measured via [O II] as the principal spectral feature. In the case of some passive galaxies, a modest Hδ 4102Å line corresponding to the Ca II H&K-based redshifts may also be observed, but not extracted independently. These spectral features were first identified visually in both 2D and 1D spectra and analyzed using two separate methods that are described below. It is important to note that spectral features and redshifts can robustly be identified without flux calibration of spectra (see further discussion in Section 5).

3.3.1. Redshifts from Cross-correlation: RVSAO

We use the Harvard Smithsonian Astrophysical Observatory's Radial Velocity (RVSAO) IRAF package (Kurtz & Mink 1998) to implement a cross-correlation analysis between our wavelength-calibrated 1D spectrum and a galaxy template spectrum. To this end, we employed a standard template, fabtemp97, that contains absorption features commonly seen in spectra of cluster member galaxies. For the low signal-to-noise ratio (S/N) data at our disposal, we use the Ca II H&K absorption lines at rest-frame wavelengths of 3968 and 3934 Å, which fall in the observer-frame wavelength range of 8800–9400 Å for the redshifts of our sample clusters. Challenges in obtaining the redshift solutions for our data set via this method are further discussed in Section 4.

3.3.2. Redshifts from Line Identification

In order to estimate redshifts as an independent probe of low-S/N, sparsely featured spectra and to substantiate our RVSAO redshift measurements in moderate- and high-S/N spectra, we use the detections of [O II] $\lambda\lambda$3727, 3729 doublet emission features, which fall in the observer-frame wavelength range of 8300–8700 Å for the redshifts of our sample clusters (see Figure 4). Since the dispersion of our 1D spectra is 2 Å/pixel, we do not expect to resolve individual lines in this doublet feature. However, the width of the features we identify as [O II] emission is consistent with a redshifted blended [O II] doublet line profile. In our analysis, we also consider the uncertainty—albeit typically subdominant—in the median wavelength of the blended [O II] doublet feature, due to the range in the [O II] doublet line ratio from varying physical conditions. In most cases where a single emission feature is used to characterize the galaxy redshift, we are able to visually confirm a 4000 Å break

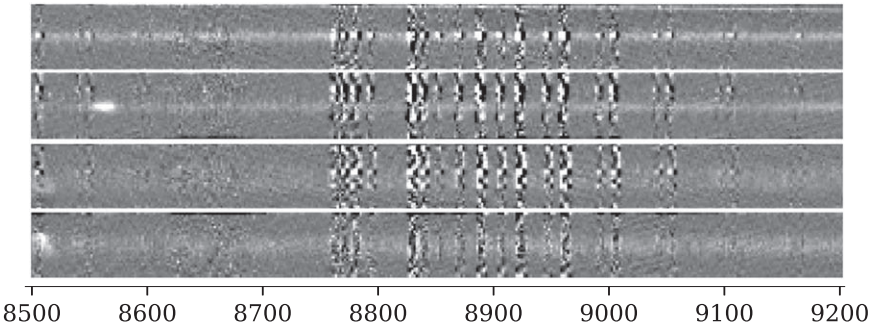

Figure 2. Example of 2D spectra used in the analysis described in Section 3, for four candidate member galaxies of the cluster SPT-CL J0156-5541. The vertical direction is the spatial dimension, and the horizontal direction is the dispersion axis, which runs from 8500 to 9200 Å from left to right. Emission features ([O II], λ3727,2729 doublet at rest frame) can be seen in the 8500–8600 Å region.

at the observed wavelength corresponding to the redshift candidate. In one case (a galaxy observed within the field of view of SPT-CL J0156-5541), this clear a diagnosis was not possible, i.e., the emission feature could potentially correspond to an [O III], Hβ, or [O II] emission peak. [O III] was disfavored because it is generally accompanied by a blueward Hβ peak, which was not observed. Hβ was ruled out because a nominal redward [O III] peak was not seen, and the existence of an [O II] peak corresponding to the cluster redshift (confirmed by 14 other cluster members in the field of view) increased our confidence in this feature being attributed to [O II].

We also independently analyze our sample spectra using a custom IDL code (from here on, customcode) designed to help identify multiple low-S/N spectral features. This custom code allows for the joint identification of multiple features by direct comparison to the data while considering both the S/N and regions contaminated by sky lines (also see Bayliss et al. 2016). We visually examined each spectrum, with typically multiple redshift solutions considered to fit apparent spectral features present in the data. Final redshifts were derived from the median of the individual line fits, with the variance providing an estimate of redshift uncertainties.

We discuss the methodology of calculating uncertainties (provided in Table 3) in Section 4.2.

4. Data Products and Results

4.1. Spectroscopic Redshifts of Member Galaxies

Table 3 contains galaxy coordinates and spectroscopic redshifts for all galaxies being considered as member galaxies for our five sample clusters. Also mentioned are the spectral features that were used to characterize the redshift. The total number of target galaxies upon which slits were placed is 109, excluding objects that serendipitously fell onto the slit. Of these, we consider 39 redshifts to be of high confidence. In addition, we include four galaxies with lower confidence redshifts that correspond to measurements with higher uncertainties than are usual for spectroscopic redshifts for galaxies ($\Delta z > 0.002$). We also include the moderately robust redshift for the BCG in SPT-CL J0607-4448 (see Section 5.2 for a detailed discussion). Inclusion of these five galaxies does not affect the scientific results of this analysis.

Figure 3 shows examples of one-dimensional spectra of four member galaxies of SPT-CL J0156-5541 at $z = 1.2935$, 1.2802, 1.2980, and 1.2900, along with 1σ pixel errors as a function of wavelength. The absorption features corresponding to Ca II H&K can be observed, indicating the presence of a dominant older stellar population.

Some of the spectra correspond to non-member galaxies (foreground or background) as well as stars. We describe non-member galaxy spectra in Table 4. This list of galaxies includes a $z = 2.48$ background galaxy with potential Fe II/Mg II outflows. This galaxy sits at a projected distance of 12″ from the SZ center of SPT-CL J0640-5113; given the mass of the cluster, this implies at least modest magnification due to lensing, though there is no indication in present data of significant shear or other suggestions of strong lensing effects. Of all the background galaxies identified, this galaxy has the most favorable geometry for strong lensing, and so we note it here for future reference. One field galaxy shows signatures of [Ne III] that may be associated with AGN activity. Another background galaxy that was spectroscopically confirmed in the field of SPT-CL J0313-5334 is a distant Lyα emitter (LAE) at $z = 6.15$; this galaxy shows little continuum in available imaging and was found as an additional source in a slit targeting a potential cluster member (itself not confirmed by these data). The observed serendipitous line shows the asymmetry typical of distant LAEs and that location on the slit shows no other spectral features, making a distant LAE the most likely interpretation.

4.2. Redshift Uncertainties

Many of the extracted 1D spectra have significant sky-subtraction residuals. Thus, a differentiation between statistical and systematic errors across the different analysis methods is needed to comprehensively quantify the redshifts.

The median cross-correlation uncertainty reported by RVSAO is $\Delta z \sim 10^{-5}$–10^{-4}, whereas the combined median line fit uncertainty (from customcode) is $\Delta z \sim 10^{-4}$–10^{-3}. The specific value and the ratio of uncertainties from the two methods for an individual spectrum depends on the S/N of the spectrum. Uncertainties in flat-fielding and wavelength calibration for these spectra also contribute to systematic uncertainties ($\Delta z \sim 10^{-4}$ each). The RVSAO code is known to underpredict uncertainties by at least a factor of 2 even absent any systematic uncertainties (Quintana et al. 2000; Bayliss et al. 2016).

Accounting for the systematic uncertainties involved requires a discussion of the RVSAO pipeline. Details of the functioning of RVSAO and physical motivations behind the algorithm are given in Kurtz & Mink (1998) and Tonry & Davis (1979), but it is worth revisiting some aspects of the pipeline and choice of parameters that are relevant to the redshift extraction at hand. RVSAO calculates redshifts based on a modified maximum-likelihood estimator that generates errors based on a cross-correlation peak width obtained from

Table 3
Spectroscopic Redshifts of Member Galaxies[a]

Cluster Name	Galaxy R.A. (J2000)	Galaxy Decl. (J2000)	z (RVSAO+[O II]+customcode)	δz	Principal Spectral Feature
(1)	(2)	(3)	(4)	(5)	(6)
SPT-CL J2341-5724	23:41:24.792	−57:25:01.25	1.2570	0.0010	Ca II H&K
SPT-CL J2341-5724	23:41:24.077	−57:24:19.71	1.2610	0.0020	Ca II H&K
SPT-CL J2341-5724	23:41:29.282	−57:26:56.12	1.2550	0.0010	Ca II H&K
SPT-CL J2341-5724	23:41:24.277	−57:24:43.50	1.2582	0.0020	Ca II H&K
SPT-CL J2341-5724	23:41:25.135	−57:25:38.42	1.2501	0.0008	Ca II H&K
SPT-CL J2341-5724	23:41:25.396	−57:26:38.72	1.2510	0.0030	Ca II H&K
SPT-CL J2341-5724	23:41:23.082	−57:25:50.93	1.2581	0.0004	Ca II H&K
SPT-CL J2341-5724	23:41:22.732	−57:25:06.47	1.2638	0.0016	Ca II H&K
SPT-CL J2341-5724	23:41:26.185	−57:24:14.38	1.2687	0.0008	Ca II H&K
SPT-CL J2341-5724	23:41:22.169	−57:25:21.68	1.2701	0.0006	Ca II H&K
SPT-CL J0156-5541	01:56:09.109	−55:42:10.51	1.2935	0.0015	Ca II H&K
SPT-CL J0156-5541	01:56:03.382	−55:43:32.36	1.2877	0.0050	[O II]
SPT-CL J0156-5541	01:56:18.665	−55:40:20.74	1.2825	0.0011	Ca II H&K/[O II]
SPT-CL J0156-5541	01:56:11.439	−55:41:18.49	1.2925	0.0030	Ca II H&K
SPT-CL J0156-5541	01:56:05.725	−55:41:57.81	1.2802	0.0009	Ca II H&K
SPT-CL J0156-5541	01:56:09.134	−55:42:19.08	1.2970	0.0030	Ca II H&K/[O II]
SPT-CL J0156-5541	01:56:12.938	−55:41:39.55	1.2925	0.0020	Ca II H&K
SPT-CL J0156-5541	01:56:17.928	−55:41:49.02	1.2980	0.0020	Ca II H&K
SPT-CL J0156-5541	01:55:55.826	−55:43:10.49	1.2830	0.0001	Ca II H&K/[O II]
SPT-CL J0156-5541	01:56:07.627	−55:40:50.23	1.2772	0.0005	Ca II H&K/[O II]
SPT-CL J0156-5541	01:56:07.438	−55:40:51.17	1.2810[b]	0.0010	[O II]
SPT-CL J0156-5541	01:55:59.089	−55:43:49.65	1.2900	0.0010	Ca II H&K
SPT-CL J0156-5541	01:55:56.724	−55:39:27.54	1.2832	0.0007	Ca II H&K/[O II]
SPT-CL J0156-5541	01:56:11.064	−55:38:31.06	1.2841	0.0020	Ca II H&K
SPT-CL J0156-5541	01:56:05.607	−55:38:42.17	1.2970	0.0005	Ca II H&K/[O II]
SPT-CL J0640-5113	06:40:17.377	−51:13:04.04	1.3180	0.0014	Ca II H&K
SPT-CL J0640-5113	06:40:18.690	−51:12:31.81	1.3120	0.0002	Ca II H&K
SPT-CL J0640-5113	06:40:23.045	−51:12:24.57	1.3264	0.0010	Ca II H&K
SPT-CL J0640-5113	06:40:16.204	−51:13:24.86	1.3031	0.0002	Ca II H&K/[O II]
SPT-CL J0640-5113	06:40:07.080	−51:13:02.32	1.3209	0.0020	Ca II H&K
SPT-CL J0640-5113	06:40:16.400	−51:12:46.13	1.3210	0.0020	Ca II H&K
SPT-CL J0640-5113	06:40:19.194	−51:14:39.36	1.3079	0.0002	Ca II H&K/[O II]
SPT-CL J0607-4448	06:07:34.218	−44:48:07.30	1.4087	0.0010	Ca II H&K
SPT-CL J0607-4448	06:07:32.462	−44:46:59.70	1.4077	0.0008	Ca II H&K
SPT-CL J0607-4448	06:07:38.712	−44:49:36.72	1.3973	0.0006	Ca II H&K
SPT-CL J0607-4448	06:07:44.442	−44:49:19.70	1.3948	0.0012	Ca II H&K
SPT-CL J0607-4448	06:07:34.824	−44:48:14.95	1.3993[c]	0.0013	[O II]
SPT-CL J0313-5334	03:13:58.536	−53:32:31.50	1.4695	0.0001	[O II]
SPT-CL J0313-5334	03:13:48.216	−53:33:48.60	1.4740	0.0010	Ca II H&K/[O II]
SPT-CL J0313-5334	03:13:58.105	−53:33:57.30	1.4881	0.0004	[O II]
SPT-CL J0313-5334	03:13:56.472	−53:34:14.61	1.4772	0.0010	Ca II H&K
SPT-CL J0313-5334	03:13:53.569	−53:35:21.12	1.4730	0.0010	Ca II H&K
SPT-CL J0313-5334	03:13:56.448	−53:35:33.50	1.4716	0.0006	Ca II H&K/[O II]
SPT-CL J0313-5334	03:13:54.049	−53:35:49.01	1.4770	0.0008	Ca II H&K/[O II]

Notes. Spectroscopic redshifts of member galaxies of sample clusters, in increasing order of the cluster redshifts. Also mentioned are the spectral features used to determine each galaxy's redshift. See Sections 3 and 4 for more details.
[a] From a combination of RVSAO cross-correlation and fit to [O II] emission features.
[b] Second trace of galaxy that fell serendipitously into the slit. Possible member galaxy.
[c] BCG of SPT-CL J0607-4448, confirmed after revisiting the spectrum (see Section 5.2 for details).

processing an input spectrum. RVSAO assumes every spectral pixel contains a flux value with uniform uncertainty, which limits our ability to interpret RVSAO output uncertainties physically, since our observed spectra have uncertainties that vary significantly with wavelength.

This is best observed in our analysis if each galaxy spectrum is run through RVSAO over multiple trials, in which most parameters are kept fixed except for the following: number of columns in which the data is rebinned in Fourier space, number of times the template spectrum is required to pass through the input galaxy spectrum, wavelength range in which cross-correlation is to be considered, initial redshift guess, and selection cutoffs for Fourier modes to be considered (highest and lowest). The results can be sensitive to these parameters, and the scatter across redshift solutions is expected to reasonably sample the systematic uncertainty. We ran multiple

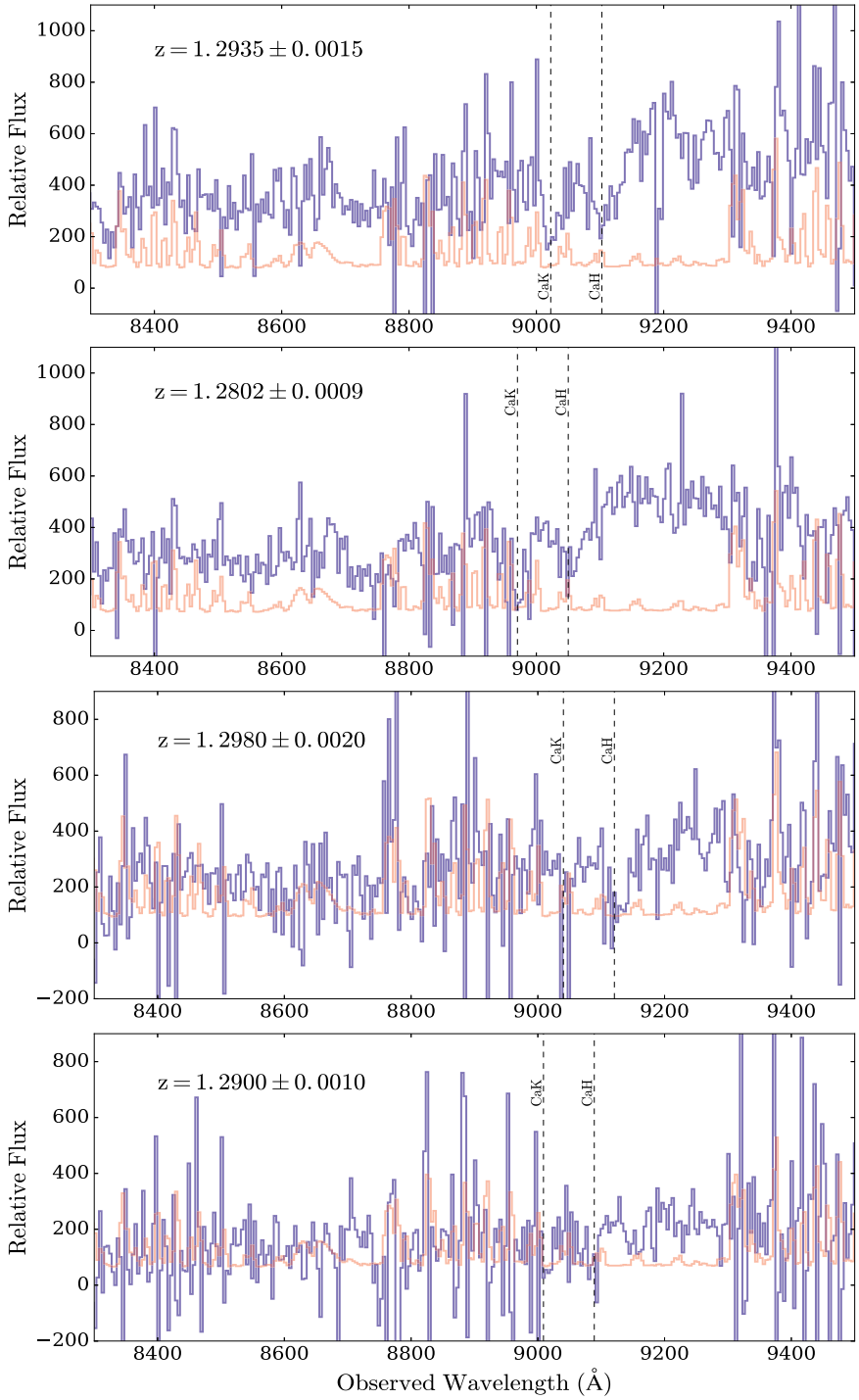

Figure 3. Extracted 1D spectra (purple) for four member galaxies of the cluster SPT-CL J0156-5541 (see Table 3), along with 1σ uncertainties (orange). Ca II H&K absorption features are indicated (black dashed lines), corresponding to robust redshift fits from RVSAO cross-correlation. Redshift values reported in this figure are final redshifts from the combined RVSAO and line identification analyses.

RVSAO trials with all parameters fixed, except cross-correlation wavelength range and initial redshift guess.

Each unique wavelength range corresponds to a single trial, used as an input to RVSAO, with different output cross-correlation peaks. Moreover, in trials with relatively small wavelength ranges, care is taken to eliminate wavelength regions of high noise.

The median scatter in output redshifts observed across multiple trials for the same galaxy spectrum is $\Delta z \sim 10^{-3}$, which matches the statistical uncertainties obtained from the customcode analysis. Keeping the wavelength range and initial redshift guess intact while changing the template spectrum (e.g., SAO's habtemp90) returns a similar range of uncertainties.

As mentioned above, in the presence of these limitations, we quote the most conservative uncertainties for individual redshifts. We start with considering median redshifts from multiple RVSAO cross-correlation trials. For RVSAO, we quote the rms uncertainties from multiple cross-correlation trials. In the few cases where [O II] emission was observed, we

Table 4
Spectroscopic Redshifts of Field Galaxies in the Data Set[a]

Spectroscopic Mask ID	Galaxy R.A. (J2000)	Galaxy Decl. (J2000)	z	δz	Principal Spectral Feature
(1)	(2)	(3)	(4)	(5)	(6)
SPT-CL J2341-5724	23:41:13.112	−57:25:49.46	1.3410	0.0100	Ca II H&K
SPT-CL J2341-5724	23:41:25.993	−57:23:52.63	1.3272[b]	0.0005	Ca II H&K
SPT-CL J2341-5724	23:41:23.041	−57:27:34.72	1.1436	0.0017	Ca II H&K/[Ne III]
SPT-CL J2341-5724	23:41:23.686	−57:22:32.03	0.8031	0.0006	Ca II H&K
SPT-CL J0640-5113	06:40:25.283	−51:13:14.46	0.6404	0.0001	[O III]
SPT-CL J0640-5113	06:40:05.611	−51:13:07.66	0.8189	0.0002	Hβ/[O III]
SPT-CL J0640-5113	06:40:16.445	−51:13:04.79	2.4840	0.0010	Fe II/Mg II
SPT-CL J0640-5113	06:40:19.209	−51:13:41.13	1.3590	0.0010	Ca II H&K
SPT-CL J0607-4448	06:07:33.586	−44:47:49.66	1.4933	0.0005	Ca II H&K
SPT-CL J0607-4448	06:07:38.992	−44:47:59.12	1.7181	0.0004	[O II]
SPT-CL J0607-4448	06:07:24.579	−44:47:26.57	1.4716	0.0011	Ca II H&K
SPT-CL J0607-4448	06:07:28.380	−44:47:03.95	1.3078	0.0013	Ca II H&K
SPT-CL J0607-4448	06:07:42.238	−44:47:37.27	1.4787	0.0004	[O II]
SPT-CL J0607-4448	06:07:42.844	−44:48:59.94	1.4965	0.0004	[O II]/Hδ
SPT-CL J0313-5334	03:13:49.369	−53:32:45.96	1.0926	0.0008	Ca II H&K/G-band
SPT-CL J0313-5334	03:13:49.369	−53:32:45.96	0.86851[b]	0.0001	[O III]/Hβ
SPT-CL J0313-5334	03:13:49.248	−53:33:07.39	1.0680	0.0001	Hg/Hβ/[O III]
SPT-CL J0313-5334	03:13:49.248	−53:33:07.39	1.3586[b]	0.0003	[O II]
SPT-CL J0313-5334	03:13:57.024	−53:33:36.79	1.3029	0.0008	[O II]
SPT-CL J0313-5334	03:13:56.472	−53:34:14.611	1.2320	0.0010	[O II]
SPT-CL J0313-5334	03:13:55.993	−53:34:24.96	1.2313	0.0003	[O II]/Hδ
SPT-CL J0313-5334	03:13:53.040	−53:35:00.24	1.2150	0.0010	[O II]
SPT-CL J0313-5334	03:13:53.982	−53:35:08.11	1.2620	0.0004	[O II]
SPT-CL J0313-5334	03:13:50.521	−53:36:02.16	6.1480	0.0010	Lyα
SPT-CL J0313-5334	03:13:56.017	−53:36:59.91	1.1591	0.0006	Ca II H&K

Notes.
[a] From a combination of RVSAO cross-correlation and line identification.
[b] A second trace of a galaxy that fell serendipitously onto the slit.

then consider the median of RVSAO cross-correlation and [O II] emission-line redshifts, with rms errors.

The results from the above analysis are then compared with the customcode uncertainties. To be consistent with our approach of reporting the most conservative errors due to presence of unquantifiable sky subtraction systematics, the largest of the three—RVSAO+[O II] uncertainties, customcode uncertainties, and the difference in redshift solutions from the two sets of analyses—is taken as the galaxy redshift uncertainty. RVSAO's ability to observe spectral features across different pixel scales (or Fourier modes) in a galaxy spectrum, the agreement in redshifts from three independent analyses, and the confirmation of redshift results by visual inspection of these spectra give us confidence in our redshift estimates and the characterization of redshift uncertainties. Moreover, individual galaxy redshift uncertainties do not have a significant effect on the primary scientific result of this work, which is the cluster redshifts.

5. Discussion

5.1. Galaxy Cluster Redshifts (and Velocity Dispersions)

Redshift estimation in this work follows the same procedure as all previous SPT follow-up studies, described in Ruel et al. (2014). It involves using the bi-weight location estimator to calculate the average redshift, $\bar{z}_{\rm cluster}$, assuming a redshift sample drawn from a Gaussian distribution. For the calculation of velocity dispersion, the bi-weight estimator is robust and resistant to outliers and low number statistics. However, in cases of very small samples ($N \leqslant 15$), the gapper estimator is preferred and is used in this work. We calculate $\bar{z}_{\rm cluster}$ as best determined using the procedure formulated in Beers et al. (1990). The line-of-sight velocity for individual galaxies is computed using the following relationship:

$$v_i = c\frac{(z_i - \bar{z}_{\rm cluster})}{(1 + \bar{z}_{\rm cluster})} \quad (1)$$

where $\bar{z}_{\rm cluster}$ is the bi-weight location-estimated mean redshift, and the denominator accounts for the difference between the emitter's rest frame and the cosmological expansion of the universe. The list of velocities v_i is used as an input to the gapper estimator to calculate the line-of-sight velocity dispersion σ_v, once $\bar{z}_{\rm cluster}$ is finalized. This gives us an initial estimate of $\sigma_{v,G}$. We then account for outliers/interlopers in velocity space by making a hard $\pm 3\sigma$ cut on the distribution of $\sigma_{v,G}$ and ejecting them from the next iteration of calculations until convergence is reached (also see Section 5.4.2). Uncertainties on $\bar{z}_{\rm cluster}$ are calculated using the following expression in Ruel et al. (2014) for estimating standard deviation (once again, assuming the measured redshifts are close to a normal distribution):

$$\Delta z = \frac{1}{c}\frac{\sigma_v(1 + \bar{z}_{\rm cluster})}{\sqrt{N_{\rm members}}} \quad (2)$$

where $\sigma_v = \sigma_{v,G}$ is the relevant gapper velocity dispersion, $1 + z$ is needed because $\sigma_{v,G}$ is defined in the rest frame, and

Table 5
Mean Redshifts, Velocity Dispersions, and Mass Comparisons of Sample Galaxy Clusters

Cluster Name	Members	z	δz	$\sigma_{v,G}$[a]	$M_{200c,\mathrm{SZ}}$[b]	$M_{200c,\mathrm{X\text{-}ray}}$[c]	$M_{200c,\mathrm{dyn}}$[d]
	(no.)			(km s^{-1})	($\times 10^{14}\ h_{70}^{-1}\ M_\odot$)	($\times 10^{14}\ h_{70}^{-1}\ M_\odot$)	($\times 10^{14}\ h_{70}^{-1}\ M_\odot$)
(1)	(2)	(3)	(4)	(5)	(6)	(7)	(8)
SPT-CL J2341-5724	10	1.2588	0.0021	941 ± 285	$4.90^{+1.00}_{-1.00}$	$5.40^{+1.20}_{-1.20}$	$5.10^{+5.90}_{-3.30}$
SPT-CL J0156-5541	15	1.2879	0.0018	936 ± 228	$5.90^{+1.20}_{-1.20}$	$6.30^{+1.00}_{-1.00}$	$4.90^{+4.40}_{-2.70}$
SPT-CL J0640-5113	7	1.3162	0.0031	1147 ± 426	$5.80^{+1.20}_{-1.20}$	$4.70^{+1.00}_{-1.00}$	$8.80^{+13.20}_{-6.50}$
SPT-CL J0607-4448	5	1.4010[e]	0.0028	843 ± 383	$5.10^{+1.10}_{-1.10}$	$4.30^{+0.90}_{-0.90}$	$3.40^{+6.80}_{-2.80}$
SPT-CL J0313-5334	7	1.4741	0.0018	727 ± 270	$4.90^{+1.10}_{-1.10}$	$3.20^{+2.60}_{-2.50}$	$2.20^{+3.20}_{-1.60}$

Notes.
[a] Using the robust and resistant gapper estimator, recommended for $N \leqslant 15$ member galaxies, described in Beers et al. (1990) and Ruel et al. (2014).
[b] SZ masses reported in B15 and scaled up to M_{200c}.
[c] X-ray temperature-based masses reported in McDonald et al. (2017).
[d] Using the gapper velocity dispersion and the M–σ_v relation (see Saro et al. 2013 for details).
[e] Cluster redshift determined out of two redshift "groups," $z = 1.40$ and $z = 1.48$. See Section 5.2 for more details.

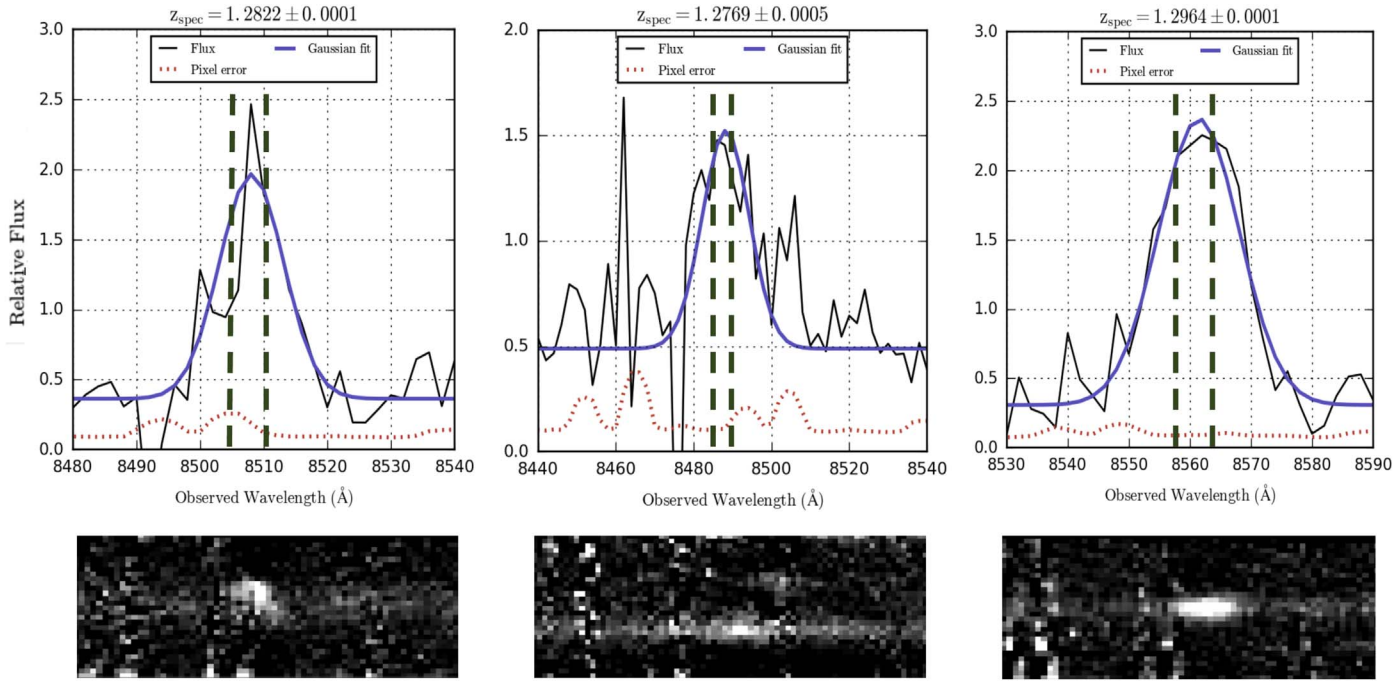

Figure 4. Upper panels: examples of individual 1D spectra (black solid line) for individual member galaxies of SPT-CL J0156-5541 (see Table 3) that show strong [O II] emission lines. Uncertainties are indicated with red dotted lines. The main emission feature reflects the emission from the [O II] 3727, 3729 doublet, which is blended at our resolution. The mean redshift (corresponding to a rest-frame wavelength of 3728.1 Å) is used to constrain spectroscopic redshifts for these galaxies. The dashed vertical lines indicate the observed wavelengths of the two lines in the [O II] doublet. The purple curves are Gaussian fits to the emission features. Lower panels: 2D spectra corresponding to the galaxies above. The lower-central panel contains two [O II]-emitting cluster members serendipitously observed with the same slit.

$1/c$ converts velocity to redshift. Jackknife and bootstrap estimates of this uncertainty also converge to this expression (Ruel et al. 2014). Confidence intervals on velocity dispersions are estimated to be

$$\Delta\sigma_v = \frac{\pm C}{\sigma_v \sqrt{N_{\mathrm{members}} - 1}} \tag{3}$$

This expression accurately captures the confidence interval on the total measurement. For the gapper statistic, $C = 0.91$.

The final redshifts and velocity dispersions are tabulated in Table 5. Figure 5 shows the distribution of individual cluster member velocities (with an overplotted Gaussian distribution of mean 0, standard deviation $\sigma_{v,G}$, and an amplitude corresponding to the maxima of the histogram bin counts), where the distribution of member galaxy velocities and the estimated values of the cluster velocity dispersions are consistent with each other.

5.2. The Curious Case of SPT-CL J0607-4448

SPT-CL J0607-4448 ($z_{\mathrm{phot}} = 1.43 \pm 0.09$, $M_{500c,\mathrm{SZ}} \sim 3.14 \pm 0.64 \times 10^{14} h^{-1}\ M_\odot$) was targeted for LDSS3 spectroscopy with 20 slits on a multiobject mask, with 10 delivering reliable redshifts (including two field galaxies not associated with the cluster). Eight of the resulting galaxy redshifts were found to be grouped around two redshifts—$z \sim 1.40$ (1.4087, 1.4077, 1.3973, and 1.3948), and $z \sim 1.48$ (1.4933, 1.4716, 1.4787, and 1.4965). These two redshift groups are separated enough along

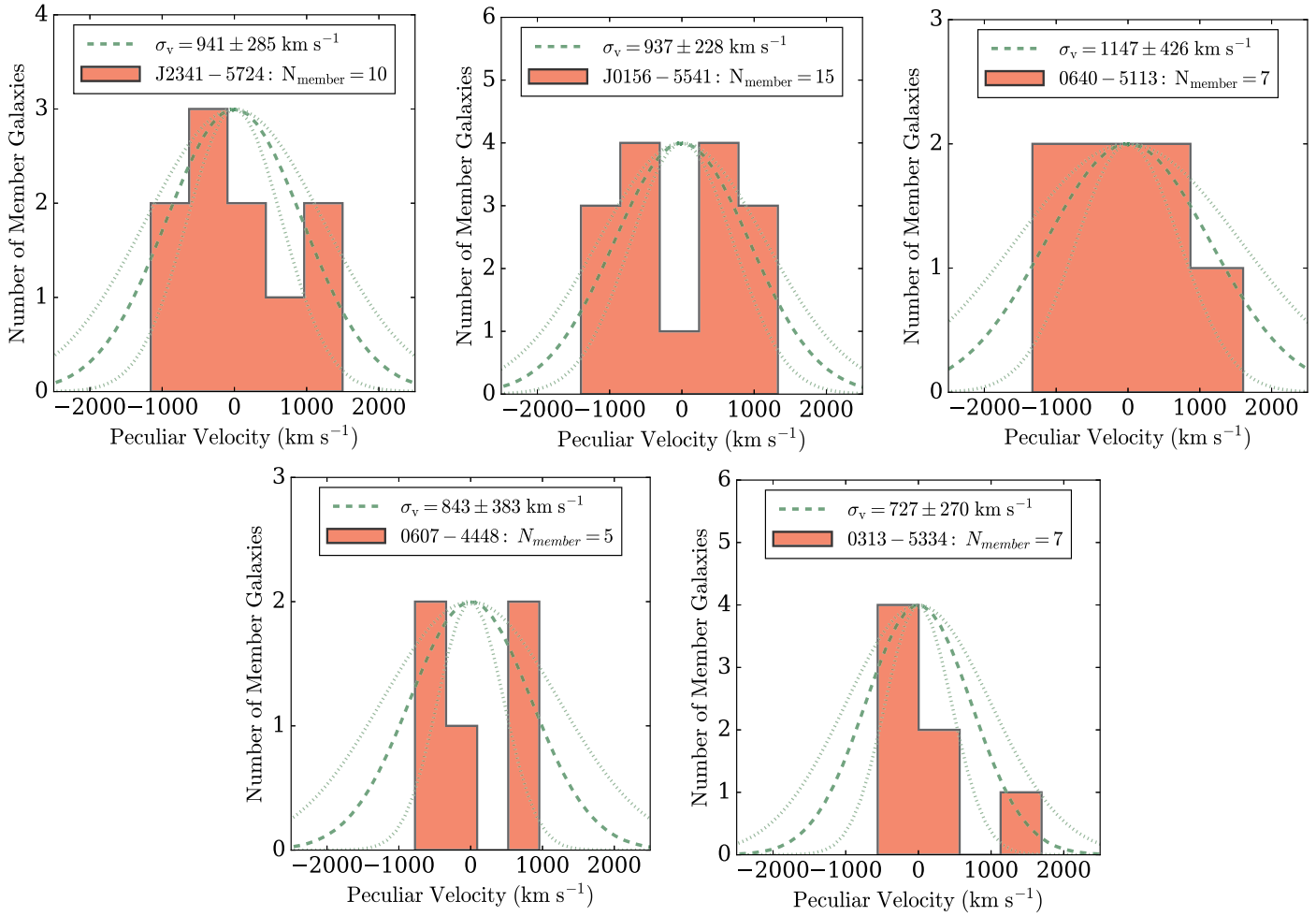

Figure 5. Histogram of peculiar velocities (in orange) from the five sample clusters (with a total of $N = 44$ galaxies with their respective peculiar velocities). Overplotted is a Gaussian distribution fit of member galaxy velocities with the standard deviation of $\sigma_{v,G}$ (in dotted green, mean with uncertainties) and a normalization factor corresponding to the maxima of bin counts. See Table 5 for details on dispersions and masses of individual galaxy clusters.

the Hubble flow that they are certainly distinct objects. However, it is unclear which object dominates the SZ signal that led to the detection of SPT-CL J0607-4448 in the SPT-SZ survey. Based on the properties of four galaxies measured in each redshift group, the velocity dispersions and member galaxy velocity distributions do not clearly favor any one candidate ($\sigma_{v,G}$ for $z \sim 1.40$ and $z \sim 1.48$ are 843 ± 383 and 1587 ± 834 km s^{-1}, respectively). While the $z \sim 1.40$ dynamics (namely, the numerical value of the velocity dispersion) are relatively more consistent with expectations and the other clusters measured in this paper, the associated large uncertainties need to be noted. The spatial distribution of spectroscopically confirmed galaxies in each group does not indicate a preference for one of the redshifts. However, the detailed photometric analysis of the stellar bump and red-sequence colors for SPT-CL J0607-4448 in V. Strazzullo et al. (2018, in preparation) favors the lower redshift solution.

The BCG spectrum (Figure 6) does not possess a spectral feature (emission or absorption) that produced a clear spectroscopic redshift, due to the presence of particularly strong sky subtraction residuals. Both customcode and the RVSAO cross-correlation fail to converge to a reliable redshift, but considered against the two choices ($z = 1.40$ or 1.48), the spectrum favors a $z = 1.40$ solution. The black vertical lines correspond to the Ca II H&K doublet feature redshift to $z = 1.40$, which is in close proximity to a potential 4000 Å feature at ∼9600 Å (as opposed to the break presenting itself at ∼9880 Å in the case of a $z = 1.48$ solution). Moreover, there is a potential emission feature at 8944 Å that, in isolation, is not compelling, but can be interpreted as [O II] emission at $z \sim 1.3993$. This indicates that the cluster redshift for SPT-CL J0607-4448 is $z = 1.4010$. The galaxies in the $z \sim 1.48$ structure (which may or may not be a virialized group or cluster) are noted in Table 4.

5.3. The SPT High-z Cluster Sample in the Context of Other Clusters in the Literature

This sample contains five high-mass, high-redshift SPT-SZ −detected galaxy clusters that have been determined photometrically to be above $z > 1.25$. From the literature, we find ∼50 confirmed galaxy clusters at $z > 1.15$, which implies that spectroscopic confirmation of clusters in our sample increases the number of clusters in this regime by 10%. The SPT high-redshift cluster sample also lies at significantly higher masses than most spectroscopically confirmed clusters at such redshifts; in the high-mass/high-redshift space bounded by the lowest mass and lowest redshift SPT-SZ clusters in this sample, these five spectroscopic confirmations roughly double the total number of confirmed clusters from all previous work.

Figure 7 depicts the distribution of M_{200c} as a function of redshift (or age of the universe) of all spectroscopically confirmed galaxy clusters at $z > 1.15$ for which masses were

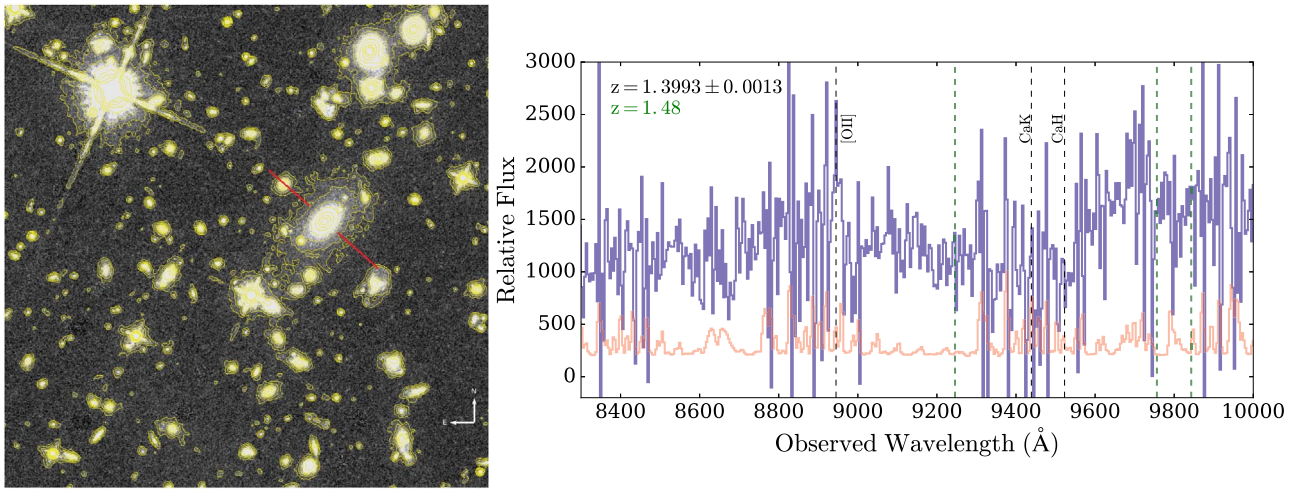

Figure 6. Left: a 500 kpc cutout of the *HST*+WFC3 F140W image (V. Strazzullo et al. 2018, in preparation) at the cluster redshift $z = 1.40$ for SPT-CL J0607-4448 centered on the SPT-SZ position. Contours are (1.25, 2.5, 5, 10, 20, 40, 60, 80, 160) times the standard deviation of the sky values, chosen to highlight low-level extended emission seen around galaxies in the image. The galaxy (indicated with red lines) has all the hallmarks of a brightest cluster galaxy (BCG); it is an early-type galaxy with an extended stellar halo larger than 100 kpc and has an appropriate color. Right: 1D spectrum for the BCG identified in the left panel. Purple corresponds to observed flux, orange is the 1σ error bars (offset for clarity). Despite absence of a clear diagnostic spectral feature for a redshift, this spectrum favors a $z = 1.40$ solution, based on the vertical green dotted lines corresponding to a redshift Ca II H&K doublet feature and a feature consistent with [O II] 3727, 3729 emission. The green dotted lines correspond to the same three spectral features, but at $z = 1.48$, clearly inconsistent with the spectrum.

reported in the literature. The census includes infrared-selected clusters from the SpARCS (Nantais et al. 2016; Noble et al. 2016), MaDCoWS (Brodwin et al. 2015; Gonzalez et al. 2015), and ISCS (Brodwin et al. 2011, 2016; Jee et al. 2011) surveys; X-ray-selected clusters from the *XMM* (Stott et al. 2010), XDCP (Fassbender et al. 2011), XLSS (Tran et al. 2015), and RDCS (Rosati et al. 1998) surveys; and SZ-selected clusters from the SPT-SZ survey. This census covers a mass range of $M_{200c} \approx 0.3$–$10 \times 10^{14} M_{\odot}$. The colors show the method used to estimate cluster mass: X-ray temperature, X-ray luminosity, SZ, and weak lensing.

The three clusters shown by red squares without black outlines are SPT-SZ clusters spectroscopically confirmed elsewhere at redshifts greater than 1.2—SPT-CL J2040-4451 ($z = 1.48$, Bayliss et al. 2014), SPT-CL J0205-5829 ($z = 1.32$, Stalder et al. 2013), and SPT-CL J0459-4947 (X-ray spectroscopy-based redshift $z = 1.70 \pm 0.02$; A. B. Mantz et al. 2018, in preparation). The red squares with black outlines represent the five SPT high-redshift clusters analyzed in this paper.

It is crucial to note that most of the redshifts confirmed in this work are derived from absorption features despite observational difficulties, while higher redshift clusters are typically confirmed by virtue of strong emission observed e.g., clusters JKCS 041 ($z = 1.8$; Andreon et al. 2014), XLSSC 122 ($z = 2.0$; Mantz et al. 2018), CL J1001+0220 ($z = 2.5$; Wang et al. 2016), and the COSMOS-ZFOURGE overdensity ($z = 2.1$; Yuan et al. 2014).

5.4. Validation of Redshift Results

As previously discussed, obtaining redshifts for primarily passively evolving galaxies at well beyond $z = 1$ is difficult, and the spectra discussed here are further compromised by systematic sky-subtraction issues. We thus consider in the subsections that follow several analyses of these data beyond cluster redshift estimation, primarily to demonstrate that the redshifts derived above are consistent with expectations for high-redshift clusters.

5.4.1. Consistency of Dynamical Masses with SZE and X-ray Masses

We estimate the dynamical masses of these five galaxy clusters using the dispersion–mass scaling relation from Saro et al. (2013):

$$M_{200c,\mathrm{dyn}} = \left(\frac{\sigma_{\mathrm{DM}}}{A \times h_{70}(z)^{C}}\right)^{B} 10^{15} M_{\odot} \quad (4)$$

where $A = 939$, $B = 2.91$, $C = 0.33$, and $M_{200c,\mathrm{dyn}}$ is the dynamical mass within R_{200c}, defined as the radius within which the mean density ρ is 200 times the critical density ρ_c of the universe. σ_{DM} is the dispersion computed from galaxy clusters in dark matter simulations, where subhalos correspond to galaxies, while $h_{70}(z)$ is the redshift-dependent Hubble constant.

It is assumed here that the average velocity dispersion of galaxies in our clusters can be substituted in the above expression, i.e., $\sigma_{\mathrm{DM}} \sim \sigma_{v,G}$, to give a crude estimate of the cluster dynamical masses, which is sufficient given the significant uncertainties associated with velocity dispersion from the small numbers of members and the uncertainty floor imposed by projection and orientation effects in individual clusters (White et al. 2010).

Additionally, other potential systematic uncertainties should be considered when comparing the dynamical mass to other estimators. An example is the conversion from $M_{500c,\mathrm{SZ}}$ to $M_{200c,\mathrm{SZ}}$ (B15 reports M_{500c})—the scale factor is ~1.65 in this redshift regime, assuming an NFW profile and a mass–concentration scaling relation from Duffy et al. (2008).

Table 5 reports the velocity dispersion, the implied dynamical masses, the SZ-derived masses (B15), and the X-ray-temperature derived masses (McDonald et al. 2017) for all five clusters. All masses are reported in M_{200c}, scaled where necessary. The dynamical mass to SZ mass ratio for this sample (calculated by fitting a line to the $M_{200c,\mathrm{dyn}}$–$M_{200c,\mathrm{SZ}}$ plane) is 0.73 ± 0.36, and the dynamical mass to X-ray mass ratio is 0.87 ± 0.42. The uncertainty in these ratios is dominated by the high uncertainties in the dynamical masses.

Figure 8 shows the masses with uncertainties for all five clusters; the dynamical masses are uncertain, but there is no evidence of deviations from expectation that would suggest any

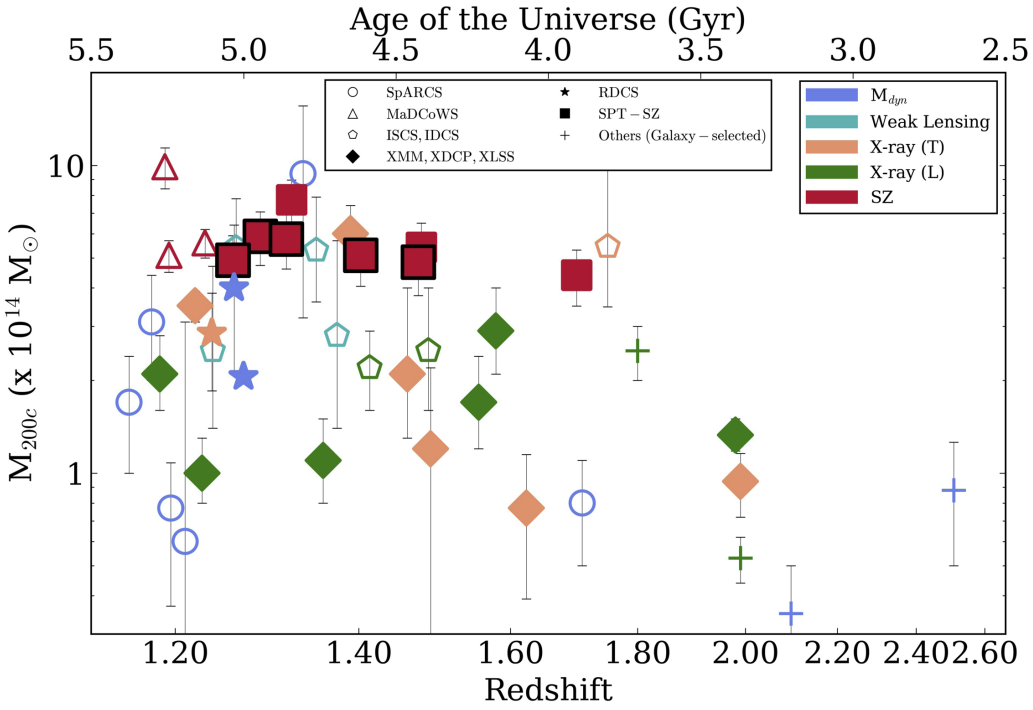

Figure 7. Mass vs. redshift (or age, in Gyr) distribution of all spectroscopically confirmed galaxy clusters with reported masses at $z > 1.15$, including clusters identified in the 2500 deg^2 SPT-SZ galaxy clusters (Bleem et al. 2015). Red filled squares correspond to the SPT High-z Cluster sample; five clusters with black outline correspond to those analyzed in this work. Also plotted are clusters from major surveys like SpARCS, MaDCoWS, and *XMM* (marked with different shapes) with their respective cluster mass measurements M_{200c} (marked with different colors). Galaxy luminosity-/color-selected clusters are represented by hollow shapes, while ICM-selected clusters are marked with filled shapes in this figure. In cases where M_{500c} is reported, M_{200c} is calculated with the assumptions of an NFW profile and a concentration $c_{500c} = 5$.

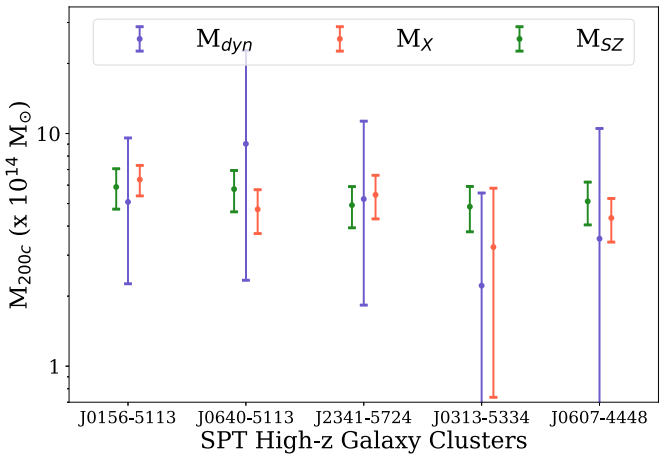

Figure 8. M_{200c} comparisons for the SPT High-z cluster sample—dynamical (purple), X-ray (orange), and SZ (green). The $M_{200c,\mathrm{dyn}}$ calculated in this paper are not inconsistent with other published masses for these galaxy clusters (see Table 5 for details).

systematic issue with the derived galaxy (and in turn, galaxy cluster) redshifts.

5.4.2. Velocity–Radius Diagrams for a Stacked Cluster

As mentioned previously, when calculating the velocity dispersion for a single cluster, we account for outliers/interlopers in velocity space by making hard $\pm 3\sigma$ cuts on the distribution of $\sigma_{v,G}$ and ejecting them from the next iteration of calculations until convergence occurs.

To examine this phase space further, we create a stacked cluster from the composite distribution of all 44 member galaxy velocities and galaxy distances from the SZ centers (the caustic technique; Diaferio & Geller 1997; Gifford et al. 2013). The SZ mass is used to normalize velocities by an equivalent dispersion $\sigma_{200c,\mathrm{SZ}}$, calculated using the dispersion–mass scaling relation (Saro et al. 2013) from $M_{200c,\mathrm{SZ}}$ (scaled up from the SPT mass $M_{500c,\mathrm{SZ}}$) akin to the previous section. The projected radial distances of individual member galaxies are also normalized by $R_{200c,\mathrm{SPT}}$. The resulting phase-space diagram is shown in Figure 9, along with the peculiar velocity distribution in the "stacked cluster." The horizontal dotted lines correspond to the $\pm 3\sigma$ threshold, while the orange dotted curve is the radially dependent $\pm 2.7\sigma(R)$ threshold from an NFW profile, for optimal interloper rejection (Mamon et al. 2010). From Figure 9, we conclude that (a) the simple 3σ outlier rejection used in Section 5.1 is sufficient and (b) the radial profile of velocities in the stacked cluster look as expected (i.e., small at the center, rising to a maximum, and decreasing at large radii), suggesting that cluster members have been robustly measured and identified. We would like to acknowledge the possibility that this radial profile evolution exhibited within the $\pm 3\sigma$ threshold can be attributed to the low number of member galaxies with confirmed redshifts.

In addition, we run a Kolmogorov–Smirnov (K-S) test on the total galaxy population's velocity distribution (gray horizontal histogram, Figure 9). The K-S statistic is 0.08, i.e., it does not reject the hypothesis that normalized galaxy velocities in our cluster sample are drawn from a Gaussian distribution. This is consistent with expectations (see Ruel et al. 2014; Bayliss et al. 2017).

We also analyze the distribution of cluster member galaxies in velocity–radius phase space by distinguishing passive (orange) from [O II]-emitting (purple) galaxies. Nominally passive galaxies describe a more centrally condensed distribution by comparison to the more extended distribution of

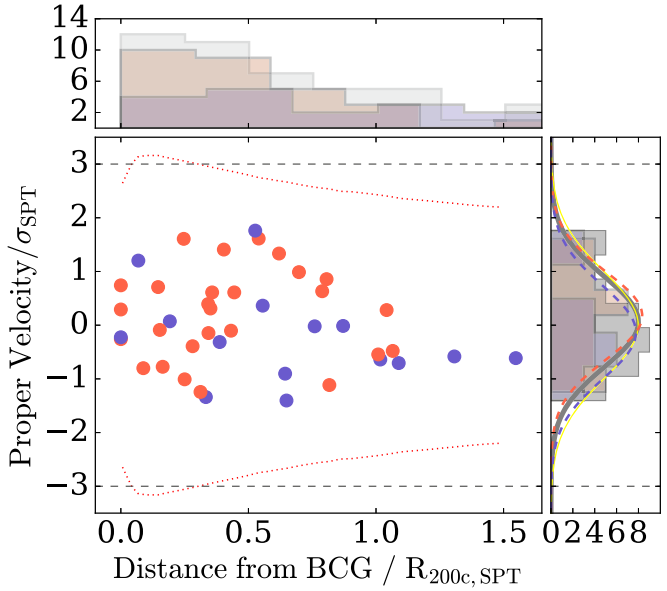

Figure 9. Normalized proper velocities vs. normalized distance of member galaxies from the SZ center, for the five sample clusters (with a total of $N = 44$ galaxies with their respective peculiar velocities) stacked as a composite cluster. Orange dots represent passive galaxies, and purple dots represent galaxies that exhibit [O II] emission (designated as non-passive galaxies). The red dotted (black dashed) contours represent the radially dependent $\pm 2.7\sigma(R)$ (hard $\pm 3\sigma$) threshold for interloper rejection. Both velocity and radius histograms show [O II]-emitting (purple), passive (orange), and total (gray) population distribution. Overplotted on the velocity histograms are Gaussian curves corresponding to the mean and standard deviation of the velocity distributions of the [O II]-emitting (dotted purple), passive (dotted orange), and all (solid gray) galaxies. The yellow curve is Gaussian, with a mean of zero and standard deviation of one. The amplitudes for the curves are arbitrary, for pictorial representation. See Table 5 for details on dispersions and masses of individual galaxy clusters.

galaxies exhibiting [O II] emission. This is likely a real trend and unlikely to be a simple selection effect—placing slits on bright red apparent cluster galaxies at larger radii is easier than in the cluster center due to less crowding, and there are potential red cluster members at all radii in the imaging data. Moreover, it is seen that the ratio of passive galaxy to [O II]-emitting galaxy velocity dispersion is 0.95 ± 0.26, in good agreement with trends observed by Bayliss et al. (2017) for low- and medium-redshift SPT-discovered galaxy clusters. This projected radius and velocity segregation between passive and emission-line galaxies is thought to indicate differences in formation timescales and accretion histories into the cluster environment (see Bayliss et al. 2017 for a comprehensive discussion). That the entire galaxy population of the stacked cluster when dissected in this manner is again consistent with expectations from lower redshift clusters also indicates that cluster member redshifts have been well measured.

5.5. Stacked Spectral Analysis of Passive Galaxies

We construct a composite spectrum of 28 passive member galaxies across the five clusters, i.e., all galaxies for which an [O II] emission feature was not detected. To stack, we shift each spectrum to the rest frame (based on its final reported redshift) and map it to the wavelength range 3645–4125 Å, with a flux normalization using the throughput curve for the instrument LDSS3C in this configuration. This is followed by a weighted-sum stacking of the 28 spectra, where each flux value is weighted by the error vector for each galaxy spectrum. We further exclude a portion of each spectrum from the stack; the excluded data are any pixels with uncertainties greater than 2× the mean uncertainty of the 10 least uncertain pixels in each input spectrum. This typically excludes about 30% of the input pixels, which roughly correspond to the majority of the pixels that have large sky-subtraction residuals.

A systematic uncertainty is calculated by varying the exclusion percentage upward and downward by 10% (i.e., typically from 20% to 40% of the pixels are excluded) in steps of 1% and computing a stacked spectrum at each cut. The variance at each pixel across the resulting 21 different stacks is taken as an estimate of the systematic uncertainty. The statistical uncertainty is calculated by bootstrapping the input spectra in the stacking process. The final reported uncertainty is the sum in quadrature of the systematic and statistical uncertainties, which typically are of comparable magnitude. The stacked spectrum (blue, with the 68% confidence interval in light blue) is shown in Figure 10.

Notably, in the stacked spectra, we detect a composite [O II] emission feature not previously detected in individual spectra. Additionally, the spectrum clearly shows a pronounced broad CN feature in the range of 3820–3850 Å, as well as Hδ absorption at 4102 Å. We also perform stellar population synthesis modeling with our stacked spectrum using the MCMC code Prospector (Conroy & Gunn 2010; Foreman-Mackey et al. 2013; Johnson & Leja 2017; Leja et al. 2017) to demonstrate that the aggregate spectrum is reasonable and as expected for cluster member galaxies at this epoch. In Figure 10, we overplot a best-fit spectrum using a simple tau (τ) model (e-folding time = 300 Myr, in orange) for a 1.7 Gyr old stellar population, at a metallicity $\log(Z/Z_{\odot}) = 0.33$ with a velocity broadening over scales of 275 km s^{-1}. Dotted lines correspond to rest-frame [O II], CN, Ca II H&K, and Hδ features. The clear emergence of [O II], Hδ, and CN features—which were not used to establish redshifts for any of these galaxies—and the overall good correspondence between the stacked and the quite reasonable model spectrum, is yet one more validation of the redshifts of the individual galaxies that were used in the composite stacking. A comprehensive analysis of physical properties of stellar populations in the cluster members characterized here shall be presented in a future paper (G. Khullar et al. 2018, in preparation).

6. Summary

We present spectroscopic follow-up of five of the most distant galaxy clusters in the 2500 deg^2 SPT-SZ survey—part of the SPT High-z Cluster sample. This work describes the observations, the spectroscopic analysis pipeline, and the data products that have been subsequently derived. We analyze this data set via cross-correlation, and manual emission and absorption-line fits, to infer robust spectroscopic redshifts for member galaxies. We argue that despite the presence of mostly low-S/N spectra dominated by sky background noise (associated with sky-subtraction residuals, an artifact of the data quality and the reduction process), useful parameters can be extracted from the data set. We perform several consistency checks for the reported spectroscopic redshifts—calculations of velocity dispersions and dynamical masses, exploration of the velocity–radius phase space for cluster member galaxies, and a composite stacked spectrum that exhibits features of nominally passive galaxies. The reported set of galaxy cluster redshifts doubles the number of galaxy clusters spectroscopically confirmed at $M_{200c} \geqslant 4.5 \times 10^{14}\, M_{\odot} h^{-1}$ and at $z > 1.2$.

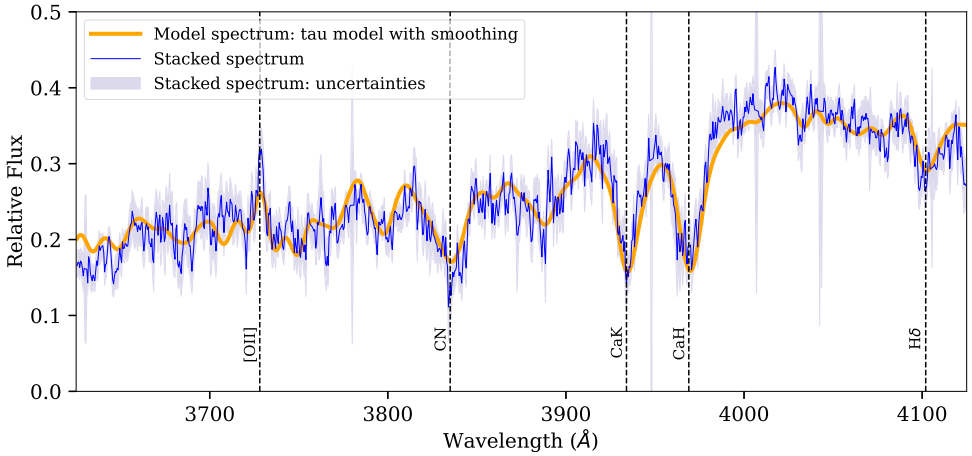

Figure 10. Stacked spectrum analysis for the 28 passive galaxies across the five clusters reported in this paper. The light blue band corresponds to 68% confidence interval based on a linear combination of statistical and systematic uncertainties in the stack. Orange spectrum corresponds to an exponential tau model of star formation that is 1.7 Gyr old, at a metallicity $\log(Z/Z_{\odot}) = +0.33$ (see Section 5.5 for a more detailed description). Dotted lines correspond to rest-frame [O II], CN, Ca II H&K, and Hδ features.

This work has been an effort to spectroscopically characterize the highest redshift massive galaxy clusters from the SPT-SZ catalog. The distant, massive cluster population presented in this work represents the progenitors of nearby massive clusters; as such, it is imperative to study this sample both observationally and in comparison with simulations. Despite limitations in spectral observations (mostly pertaining to quantifying systematics in sky subtraction), as this work reports robust cluster redshifts, future spectroscopy of these distant and faint clusters would be able to employ techniques with optimal sky subtraction (e.g., the nod-and-shuffle mode on Magellan/LDSS3 targets a narrower spectral range but is an improved handling of systematics; see Glazebrook & Bland-Hawthorn 2001). This spectroscopic confirmation study encourages further follow-up that targets observations of star formation rates and history, tracers of cluster dynamics, and estimation of velocity segregation and biases in these unique systems.

G.K. thanks Chihway Chang, Philip Mansfield, Andrey Kravtsov, Richard Kron, and Huan Lin for their helpful and thoughtful feedback that improved the analysis in this paper. G.K. would like to express gratitude toward the staff and workers at the 6.5 m Magellan Telescopes at the Las Campanas Observatory, Chile, for their valuable labor. We would also like to thank the anonymous referee whose feedback was vital in improving this manuscript. This paper has gone through internal review by the South Pole Telescope collaboration.

This work is supported by the Department of Astronomy and Astrophysics at the University of Chicago, NSF Physics Frontier Center grant PHY-1125897 to the Kavli Institute of Cosmological Physics at the University of Chicago, as well as by the Kavli Foundation, and the Gordon and Betty Moore Foundation grant GBMF 947. The South Pole Telescope is supported by the National Science Foundation through grant PLR-1248097.

B.B. is supported by Fermi Research Alliance, LLC, under contract No. DE-AC02-07CH11359 with the U.S. Department of Energy, Office of Science, Office of High Energy Physics. Argonne National Laboratory work was supported under U.S. Department of Energy contract DE-AC02-06CH11357. M.B. was supported by National Science Foundation through grant AST-1009012. A.S. is supported by the ERC-StG "ClustersXCosmo," grant agreement 71676. The data analyzed in this paper was taken on the 6.5 m Magellan Telescopes at the Las Campanas Observatory, Chile, supported by the Carnegie Observatories. This work is partly based on observations made with the NASA/ESA *Hubble Space Telescope*, obtained at the Space Telescope Science Institute, which is operated by the Association of Universities for Research in Astronomy, Inc., under NASA contract NAS 5-26555, associated with SPT follow-up GO program 14252. This work is based in part on observations made with the *Spitzer Space Telescope*, which is operated by the Jet Propulsion Laboratory, California Institute of Technology under a contract with NASA. C.R. acknowledges support from the Australian Research Council's Discovery Projects scheme (DP150103208).

Facilities: SPT, Magellan:Clay (LDSS3, PISCO), Magellan:Baade (IMACS, FOURSTAR), *CXO*, *Spitzer*, *HST*.

Software: COSMOS, Python—Numpy, Scipy, Astropy (The Astropy Collaboration et al. 2018), Colossus, Matplotlib, Pandas, Python-fsps, Prospector, emcee, IRAF- NOAO,RVSAO.

ORCID iDs

G. Khullar https://orcid.org/0000-0002-3475-7648
M. B. Bayliss https://orcid.org/0000-0003-1074-4807
M. McDonald https://orcid.org/0000-0001-5226-8349
D. E. Applegate https://orcid.org/0000-0001-8322-4672
M. L. N. Ashby https://orcid.org/0000-0002-3993-0745
S. Bocquet https://orcid.org/0000-0002-4900-805X
M. Brodwin https://orcid.org/0000-0002-4208-798X
T. M. Crawford https://orcid.org/0000-0001-9000-5013
A. H. Gonzalez https://orcid.org/0000-0002-0933-8601
J. Hlavacek-Larrondo https://orcid.org/0000-0001-7271-7340
H. Hoekstra https://orcid.org/0000-0002-0641-3231
A. von der Linden https://orcid.org/0000-0002-3881-7724
C. L. Reichardt https://orcid.org/0000-0003-2226-9169
K. Sharon https://orcid.org/0000-0002-7559-0864
B. Stalder https://orcid.org/0000-0003-0973-4900
A. A. Stark https://orcid.org/0000-0002-2718-9996

References

Alberts, S., Pope, A., Brodwin, M., et al. 2014, MNRAS, 437, 437
Alberts, S., Pope, A., Brodwin, M., et al. 2016, ApJ, 825, 72

Andreon, S., Newman, A. B., Trinchieri, G., et al. 2014, A&A, 565, A120
Balogh, M. L., Gilbank, D. G., Muzzin, A., et al. 2017, MNRAS, 470, 4168
Balogh, M. L., Morris, S. L., Yee, H. K. C., Carlberg, R. G., & Ellingson, E. 1997, ApJL, 488, L75
Bartalucci, I., Arnaud, M., Pratt, G. W., & Le Brun, A. M. C. 2018, A&A, 617, A64
Bayliss, M. B., Ashby, M. L. N., Ruel, J., et al. 2014, ApJ, 794, 12
Bayliss, M. B., Ruel, J., Stubbs, C. W., et al. 2016, ApJS, 227, 3
Bayliss, M. B., Zengo, K., Ruel, J., et al. 2017, ApJ, 837, 88
Beers, T. C., Flynn, K., & Gebhardt, K. 1990, AJ, 100, 32
Blanton, M. R., & Moustakas, J. 2009, ARA&A, 47, 159
Bleem, L. E., Stalder, B., de Haan, T., et al. 2015, ApJS, 216, 27
Brodwin, M., Brown, M. J. I., Ashby, M. L. N., et al. 2006, ApJ, 651, 791
Brodwin, M., Greer, C. H., Leitch, E. M., et al. 2015, ApJ, 806, 26
Brodwin, M., McDonald, M., Gonzalez, A. H., et al. 2016, ApJ, 817, 122
Brodwin, M., Ruel, J., Ade, P. A. R., et al. 2010, ApJ, 721, 90
Brodwin, M., Stanford, S. A., Gonzalez, A. H., et al. 2013, ApJ, 779, 138
Brodwin, M., Stern, D., Vikhlinin, A., et al. 2011, ApJ, 732, 33
Bruzual, A. G., & Charlot, S. 1993, ApJ, 405, 538
Carlstrom, J. E., Ade, P. A. R., Aird, K. A., et al. 2011, PASP, 123, 568
Carlstrom, J. E., Holder, G. P., & Reese, E. D. 2002, ARA&A, 40, 643
Conroy, C., & Gunn, J. E. 2010, ApJ, 712, 833
Culverhouse, T. L., Bonamente, M., Bulbul, E., et al. 2010, ApJL, 723, L78
Demarco, R., Wilson, G., Muzzin, A., et al. 2010, ApJ, 711, 1185
Diaferio, A., & Geller, M. J. 1997, ApJ, 481, 633
Dressler, A. 1980, ApJ, 236, 351
Dressler, A., & Gunn, J. E. 1983, ApJ, 270, 7
Duffy, A. R., Schaye, J., Kay, S. T., & Dalla Vecchia, C. 2008, MNRAS, 390, L64
Eisenhardt, P. R. M., Brodwin, M., Gonzalez, A. H., et al. 2008, ApJ, 684, 905
Elston, R. J., Gonzalez, A. H., McKenzie, E., et al. 2006, ApJ, 639, 816
Fassbender, R., Böhringer, H., Nastasi, A., et al. 2011, NJPh, 13, 125014
Flaugher, B., Diehl, H. T., Honscheid, K., et al. 2015, AJ, 150, 150
Foreman-Mackey, D., Hogg, D. W., Lang, D., & Goodman, J. 2013, PASP, 125, 306
Gettings, D. P., Gonzalez, A. H., Stanford, S. A., et al. 2012, ApJL, 759, L23
Gifford, D., Miller, C., & Kern, N. 2013, ApJ, 773, 116
Glazebrook, K., & Bland-Hawthorn, J. 2001, PASP, 113, 197
Gonzalez, A. H., Decker, B., Brodwin, M., et al. 2015, ApJL, 812, L40
Hilton, M., Hasselfield, M., Sifón, C., et al. 2018, ApJS, 235, 20
Hilton, M., Stanford, S. A., Stott, J. P., et al. 2009, ApJ, 697, 436
Holden, B. P., van der Wel, A., Franx, M., et al. 2005, ApJL, 620, L83
Jee, M. J., Dawson, K. S., Hoekstra, H., et al. 2011, ApJ, 737, 59
Johnson, B., & Leja, J. 2017, bd-j/prospector: Initial Release, Zenodo, 10.5281/zenodo.1116491
Kelson, D. D. 2003, PASP, 115, 688
Kurtz, M. J., & Mink, D. J. 1998, PASP, 110, 934
Leja, J., Johnson, B. D., Conroy, C., van Dokkum, P. G., & Byler, N. 2017, ApJ, 837, 170
Mamon, G. A., Biviano, A., & Murante, G. 2010, A&A, 520, A30
Mancone, C. L., Baker, T., Gonzalez, A. H., et al. 2012, ApJ, 761, 141
Mancone, C. L., Gonzalez, A. H., Brodwin, M., et al. 2010, ApJ, 720, 284
Mantz, A. B., Abdulla, Z., Allen, S. W., et al. 2018, A&A, 620, A2
McDonald, M., Allen, S. W., Bayliss, M., et al. 2017, ApJ, 843, 28
McDonald, M., Benson, B. A., Vikhlinin, A., et al. 2013, ApJ, 774, 23
Mei, S., Holden, B. P., Blakeslee, J. P., et al. 2006, ApJ, 644, 759
Mullis, C. R., Rosati, P., Lamer, G., et al. 2005, ApJL, 623, L85
Muzzin, A., Wilson, G., Yee, H. K. C., et al. 2009, ApJ, 698, 1934
Nantais, J. B., van der Burg, R. F. J., Lidman, C., et al. 2016, A&A, 592, A161
Noble, A. G., Webb, T. M. A., Yee, H. K. C., et al. 2016, ApJ, 816, 48
Oemler, A., Jr. 1974, ApJ, 194, 1
Papovich, C., Momcheva, I., Willmer, C. N. A., et al. 2010, ApJ, 716, 1503
Paterno-Mahler, R., Blanton, E. L., Brodwin, M., et al. 2017, ApJ, 844, 78
Planck Collaboration, Ade, P. A. R., Aghanim, N., et al. 2014, A&A, 571, A20
Quintana, H., Carrasco, E. R., & Reisenegger, A. 2000, AJ, 120, 511
Reichardt, C. L., Stalder, B., Bleem, L. E., et al. 2013, ApJ, 763, 127
Rosati, P., Della Ceca, R., Norman, C., & Giacconi, R. 1998, ApJL, 492, L21
Rosati, P., Tozzi, P., Ettori, S., et al. 2004, AJ, 127, 230
Rosati, P., Tozzi, P., Gobat, R., et al. 2009, A&A, 508, 583
Ruel, J., Bazin, G., Bayliss, M., et al. 2014, ApJ, 792, 45
Santos, J. S., Tozzi, P., & Rosati, P. 2011, MSAIS, 17, 66
Saro, A., Mohr, J. J., Bazin, G., & Dolag, K. 2013, ApJ, 772, 47
Sifón, C., Battaglia, N., Hasselfield, M., et al. 2016, MNRAS, 461, 248
Snyder, G. F., Brodwin, M., Mancone, C. M., et al. 2012, ApJ, 756, 114
Song, J., Zenteno, A., Stalder, B., et al. 2012, ApJ, 761, 22
Stalder, B., Ruel, J., Šuhada, R., et al. 2013, ApJ, 763, 93
Stalder, B., Stark, A. A., Amato, S. M., et al. 2014, Proc. SPIE, 9147, 91473Y
Stanford, S. A., Brodwin, M., Gonzalez, A. H., et al. 2012, ApJ, 753, 164
Stanford, S. A., Eisenhardt, P. R., Brodwin, M., et al. 2005, ApJL, 634, L129
Stanford, S. A., Eisenhardt, P. R., & Dickinson, M. 1998, ApJ, 492, 461
Stanford, S. A., Gonzalez, A. H., Brodwin, M., et al. 2014, ApJS, 213, 25
Stanford, S. A., Romer, A. K., Sabirli, K., et al. 2006, ApJL, 646, L13
Staniszewski, Z., Ade, P. A. R., Aird, K. A., et al. 2009, ApJ, 701, 32
Stott, J. P., Collins, C. A., Sahlén, M., et al. 2010, ApJ, 718, 23
The Astropy Collaboration, Price-Whelan, A. M., Sipócz, B. M., et al. 2018, AJ, 156, 123
Tonry, J., & Davis, M. 1979, AJ, 84, 1511
Tran, K.-V. H., Nanayakkara, T., Yuan, T., et al. 2015, ApJ, 811, 28
Tran, K.-V. H., Papovich, C., Saintonge, A., et al. 2010, ApJL, 719, L126
Vanderlinde, K., Crawford, T. M., de Haan, T., et al. 2010, ApJ, 722, 1180
Wang, T., Elbaz, D., Daddi, E., et al. 2016, ApJ, 828, 56
White, M., Cohn, J. D., & Smit, R. 2010, MNRAS, 408, 1818
Williamson, R., Benson, B. A., High, F. W., et al. 2011, ApJ, 738, 139
Wilson, G., Muzzin, A., Lacy, M., et al. 2006, arXiv:astro-ph/0604289
Yuan, T., Nanayakkara, T., Kacprzak, G. G., et al. 2014, ApJL, 795, L20
Zeimann, G. R., Stanford, S. A., Brodwin, M., et al. 2012, ApJ, 756, 115